Microporous and Mesoporous Materials 156 (2012) 217–223

Contents lists available at SciVerse ScienceDirect

Microporous and Mesoporous Materials

journal homepage: www.elsevier.com/locate/micromeso

Short Communication

Adsorptive separation of $CO_2/CH_4/CO$ gas mixtures at high pressures

Rajamani Krishna *

Van 't Hoff Institute for Molecular Sciences, University of Amsterdam, Science Park 904, 1098 XH Amsterdam, The Netherlands

ARTICLE INFO

Article history:
Received 30 November 2011
Received in revised form 13 February 2012
Accepted 18 February 2012
Available online 3 March 2012

Keywords:
CO_2 removal
Pressure swing adsorption
Metal organic frameworks
Zeolites
Selectivities

ABSTRACT

The major objective of this communication is to compare the performance of three metal–organic frameworks (MOFs): CuBTC, MIL-101, and Zn(bdc)dabco, with that of NaX zeolite for selective adsorption of CO_2 from mixtures containing CH_4 and CO in a pressure swing adsorption (PSA) unit operating at pressures ranging to 60 bar. Data on the pure component adsorption isotherms in the published literature are available in terms of *excess* loadings. For purposes of isotherm fitting with fundamental Langmuir-type models, these data need to be converted to *absolute* loadings. Calculations using the Ideal Adsorbed Solution Theory (IAST), using the fitted isotherm data on absolute loadings, show that the CO_2/CH_4 and CO_2/CO selectivities are significantly higher with NaX than for the three MOFs. The working capacity for CO_2 adsorption, on the other hand, is significantly higher for MOFs than for NaX zeolite as the pressures are increased significantly above 2 bar. For a realistic comparison of the separation characteristics in a fixed bed adsorber unit, transient breakthrough calculations were performed for an equilibrium packed bed adsorber. For a specified purity of CO_2 exiting the packed bed adsorber, the best CO_2 removal performance is obtained with CuBTC. Our studies highlight the relative importance of adsorption selectivities and capacities in the performance of fixed bed adsorbers, and underline the significant advantage of MOFs over traditionally used zeolites.

1. Introduction

In recent years there has been considerable research on the use of zeolites, metal organic frameworks (MOFs), and zeolitic imidazolate frameworks (ZIFs) for selective adsorption of CO_2 from CO_2/H_2, CO_2/CH_4 and CO_2/N_2 mixtures [1–14]. In applications such as natural gas sweetening, and H_2 purification the operating pressures can range up to 60 bar [15].

Significantly fewer studies have been devoted to separation of gas mixtures containing CO [16–23]. The adsorptive separation of CO_2 from CO is of particular interest to NASA's MARS in-situ resource utilization program [23]. The industrial need for separation of $CO_2/CH_4/CO$ gas mixtures has been underlined by Hamon et al. [20]. Hydrogen is mainly produced by steam reforming of natural gas, a process which generates a synthesis gas mixture containing H_2, CO_2, CO, and CH_4. In order to obtain pure H_2, pressure swing adsorption (PSA) is used to remove these impurities from the synthesis gas mixture. In practice, the adsorbed impurities (CO_2, CO, and CH_4) are then recovered from the column by desorption at lower pressures. The $CO_2/CH_4/CO$ purge gas is normally used for combustion purposes in a steam reformer. In view of the current concerns about CO_2 emissions there is an incentive to remove CO_2 from the purge gas mixture. After selective adsorption of CO_2 from the purge gas, the recovered CO and CH_4 are usable as fuel gas in the steam reformer.

For evaluation of suitable adsorbents for selective removal of CO_2 from mixtures containing CO and CH_4, pure component adsorption isotherm data are required. Experimental isotherm data, in terms of *excess* loadings, are available for a variety of MOFs: CuBTC [21], MIL-101 [21], and Zn(bdc)dabco [22] for pressures ranging to 100 bar. The corresponding data for conventionally used NaX zeolite is available in the works of Belmabkhout et al. [16] and Cavenati et al. [24]. Isotherm fitting with fundamental models, such as Langmuir and Toth, should be done using *absolute*, not *excess*, loadings; this has been stressed by Myers and Monson [25]. The poorer the adsorption strength, the larger is the difference between the absolute and excess loadings; the differences are particularly significant for poorly adsorbing gases such as H_2 and N_2. Isotherm fits of absolute loadings need to be used for calculations of the adsorption selectivity, S_{ads}, using say the Ideal Adsorbed Solution Theory (IAST) of Myers and Prausnitz [26]. Indeed, in several recent investigations [1–3,11,15,27,28], the experimental data have been first converted from excess to absolute loadings, prior to isotherm fitting and subsequent use in IAST calculations of S_{ads}, and breakthrough simulations of PSA performance. Regretfully, the excess loading data for CO_2, CH_4, and CO isotherms in CuBTC, MIL-101, and Zn(bdc)dabco have been fitted directly by Chowdhury et al. [21] and Mishra et al. [22] without first conversion to absolute loadings. This implies that their reported isotherm fit parameters are not directly usable.

* Tel.: +31 20 6270990; fax: +31 20 5255604.
E-mail address: r.krishna@uva.nl

1387-1811/$ - see front matter © 2012 Elsevier Inc. All rights reserved.
doi:10.1016/j.micromeso.2012.02.034

Nomenclature

L	length of packed bed adsorber, m
p_i	partial pressure of species i in mixture, Pa
p_t	total system pressure, Pa
q_i	component molar loading of species i, mol kg^{-1}
Q_{st}	isosteric heat of adsorption, J mol^{-1}
R	gas constant, 8.314 J mol^{-1} K^{-1}
S_{ads}	adsorption selectivity, dimensionless
t	time, s
T	absolute temperature, K
u	superficial gas velocity in packed bed adsorber, m s^{-1}
z	distance along the adsorber, m

Greek letters

ε	voidage of packed bed, dimensionless
ρ	framework density, kg m^{-3}
τ	time, dimensionless
τ_{break}	breakthrough time, dimensionless

Subscripts

i	referring to component i
t	referring to total mixture

The present communication has three main objectives. The first objective is to demonstrate the need for converting experimental data from excess to absolute loadings before fitting with Langmuir-type models. We aim to show that this conversion is essential for calculations of S_{ads}, and isosteric heats of adsorption, Q_{st}; this aspect appears to be insufficiently appreciated in some of the published literature analyzing high pressure adsorption data [13,21,22], while others have been careful in converting excess loadings to absolute loadings for the purposes of calculating Q_{st} and S_{ads} [2,3,11,15,28–30]. The second objective is to underscore the fallacy in selecting materials purely based on selectivity considerations; this need arise in view of the growing research in MOFs for which selectivity considerations are often used for screening purposes [31]. The third objective is to emphasize the importance of capacity considerations especially for high pressure separations. To achieve these objectives we examine the separation performance of CuBTC, MIL-101, Zn(bdc)dabco, and NaX for CO_2 removal from $CO_2/CH_4/CO$ mixtures by performing breakthrough calculations in a packed bed adsorber, representative of the adsorption phase of a pressure swing adsorption (PSA) unit.

Details and methodology of isotherm fitting, tabulated isotherm fit parameters, along with calculations of S_{ads}, Q_{st}, and adsorber breakthrough for the chosen microporous materials have been provided in the Supplementary material accompanying this publication. The discussions below serve to highlight the major issues that emerge from our studies.

2. Absolute and excess loadings, calculations of Q_{st} and S_{ads}

The differences between absolute and excess loading depends on a variety of factors that include pore volume, and bulk gas pressure. As illustration, Fig. 1 compares absolute and excess loadings for adsorption of CO in CuBTC, MIL-10, and Zn(bdc)dabco that have pore volumes, respectively, of 0.75, 1.38, and 0.67 cm^3 g^{-1}. For MIL-101, that has the highest pore volume the absolute loadings are about 50% larger than the excess loadings of CO for pressures higher than 60 bar; a similar conclusion holds for adsorption of CH_4. For CO_2, that has a higher adsorption strength, the differences between absolute and excess loadings are expected to be lower; see Supplementary material for quantitative information. The experimental data of Moellmer et al. [30] shows that for adsorption of weakly adsorbing H_2 in CuBTC, the absolute loadings can be more than twice the excess loadings for pressures approaching 50 MPa.

One consequence of the foregoing is that estimations of the adsorption selectivity, defined by

$$S_{ads} = \frac{q_1/q_2}{p_1/p_2} \tag{1}$$

will be overly optimistic for CO_2/CO and CO_2/CH_4 mixtures if these are based on isotherm fits of excess loadings. To illustrate this, we compared the estimates of S_{ads} for equimolar binary CO_2/CO mixture ($p_1 = p_2$) for Zn(bdc)dabco, using our fits of absolute loadings, with those reported by Mishra et al. [22], which were based on Virial fits of excess loadings; see Fig. 2. At a bulk gas pressure of 10 bar, our estimates of S_{ads} is 9, as compared to their estimates which are about 60% higher.

The isosteric heat of adsorption, Q_{st}, are usually estimated from the isotherm fits using the Clausius–Clapeyron equation

$$Q_{st} = -RT^2\left(\frac{\partial \ln p}{\partial T}\right)_q \tag{2}$$

Strictly speaking, the derivative in Eq. (2) is to be determined with the *absolute* loading, q, held constant; see Myers and Monson [25]. Moellmer et al. [30] have been meticulous in their calculations of the isosteric heats of adsorption of CO_2, CH_4, N_2 and H_2 in CuBTC and the absolute loadings are held constant in applying Eq. (2). However, in the work of Chowdhury et al. [21] and Mishra et al. [22], the isosteric heats are calculated using fits of excess loadings. By implication, their values are obtained with derivatives in which the *excess loadings* are held constant. Their calculated values of the isosteric heats of adsorption are expected to be different to those obtained in this work. This expectation is fulfilled as evidenced in Fig. 3 that compares the calculations of Q_{st} obtained in this work, with those reported by Chowdhury et al. [21] and Mishra et al. [22]. There are significant differences in the two sets of values for all three MOFs. For CuBTC and Zn(bdc)dabco the differences are apparent only at higher loadings. For MIL-101, there are significant differences over the entire range of loadings. The reason for this can be traced to the significantly higher pore volume for MIL-101 which results in a significantly large difference between excess and absolute loadings over a wide range of operating pressures.

3. Evaluation of adsorbents for $CO_2/CH_4/CO$ separation

We now address the question: which is the best adsorbent for selective removal of CO_2 from the ternary $CO_2/CH_4/CO$ mixture? The most commonly used procedure for comparing adsorbents is on the basis of the adsorption selectivity. For a arbitrarily chosen temperature of 300 K, Fig. 4a and b shows the IAST calculations of CO_2/CH_4 and CO_2/CO selectivities for a range of operating pressures using four different materials. In both cases, NaX zeolite is found to have the highest selectivities over the entire range of pressures. The conventional wisdom would be to assume that NaX is the best adsorbent. However, the performance of a PSA unit is dictated not only by S_{ads} but also by the working capacity, as has been emphasized in several publications [1,2,15,27,32–34]. Let us define the working capacity for selective adsorption of CO_2 from $CO_2/CH_4/CO$ gas mixtures as the component loading of CO_2 in the

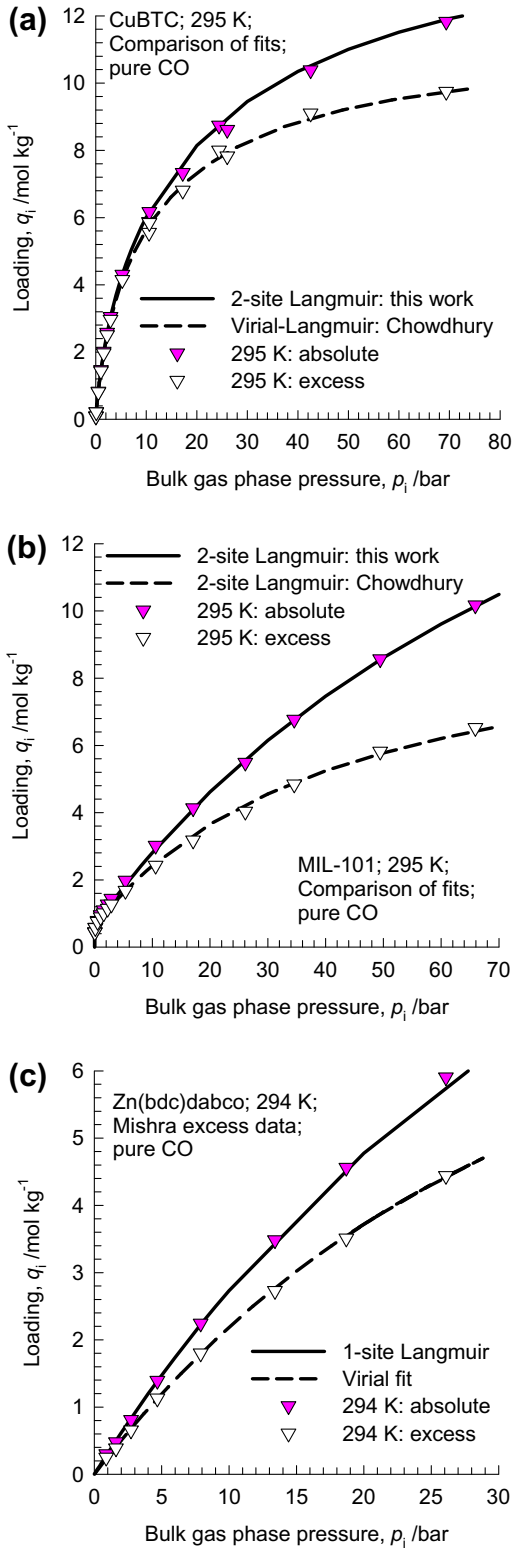

Fig. 1. Pure component isotherm data for CO in (a) CuBTC, (b) MIL-101, (c) Zn(bdc)dabco. The absolute and excess loadings are plotted in these diagrams. The continuous solid lines represent the fits of the absolute loadings from this work. The dashed lines are the fits of Chowdhury et al. [21] and Mishra et al. [22] for the excess loadings.

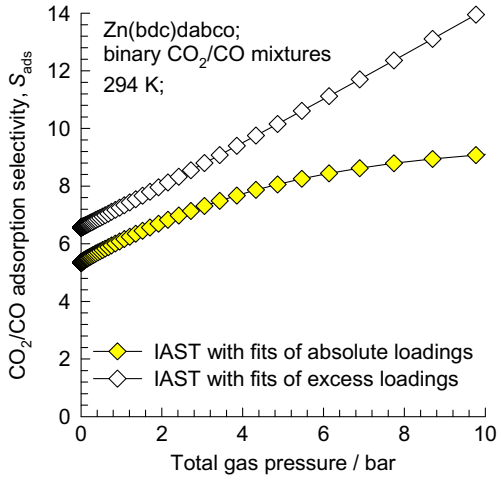

Fig. 2. Calculations of the CO_2/CO adsorption selectivities, S_{ads}, for equimolar CO_2/CO gas mixtures at 294 K using Zn(bdc)dabco. The calculations are based on the Ideal Adsorbed Solution Theory (IAST) using the pure component isotherm fits of either absolute loadings (this work) or excess loadings (obtained from the work of Mishra et al. [22]).

mixture at the operating pressure minus the value at a desorption pressure of 0.1 bar. Fig. 5 compares the working capacities for CuBTC, MIL-101, Zn(bdc)dabco, and NaX, expressed as the number of moles of CO_2 in the adsorbed mixture per L of adsorbent. With increasing pressures, the working capacity of NaX tends to reach plateau values, because saturation conditions are reached. This is because of the relatively low pore volume of NaX (0.28 cm^3 g^{-1}) compared to the much higher pore volumes of the three MOFs.

The information presented in Figs. 4 and 5 underline the dilemma faced in adsorbent selection. NaX has the best selectivities, but is limited by capacity considerations for operation at pressures exceeding 1 bar. In order to resolve the adsorbent selection dilemma we need to consider the breakthrough characteristics in a packed bed adsorber. The breakthrough calculations were performed using the methodology described in our earlier papers [27,35]. Assuming plug flow of CO_2/CH_4/CO gas mixture through a fixed bed maintained under isothermal conditions, the partial pressures in the gas phase at any position and instant of time are obtained by solving the following set of partial differential equations for each of the species i in the gas mixture.

$$\frac{1}{RT}\varepsilon\frac{\partial p_i(t,z)}{\partial t} = -\frac{1}{RT}\frac{\partial (u(t,z)p_i(t,z))}{\partial z} - (1-\varepsilon)\rho\frac{\partial q_i(t,z)}{\partial t}; \quad i = 1,2,3 \tag{3}$$

In Eq. (3), t is the time, z is the distance along the adsorber, ρ is the framework density, ε is the bed voidage, and u is the superficial gas velocity. The adsorber bed is initially free of adsorbates, i.e. we have the initial condition

$$t = 0; \quad q_i(0,z) = 0 \tag{4}$$

At time, $t = 0$, the inlet to the adsorber, $z = 0$, is subjected to a step input of the ternary gas mixture and this step input is maintained till the end of the adsorption cycle when steady-state conditions are reached.

$$t \geq 0; \quad p_i(0,t) = p_{i0}; \quad u(0,t) = u_0 \tag{5}$$

where u_0 is the superficial gas velocity at the inlet to the adsorber.

Invoking the constraint of negligible pressure drop, the overall material balance is obtained by summing Eq. (3) over the three component species

$$\frac{1}{RT}p_t\frac{\partial (u(t,z))}{\partial z} = -(1-\varepsilon)\rho\sum_{i=1}^{3}\frac{\partial q_i(t,z)}{\partial t} \tag{6}$$

Eq. (6) allows the calculation of the superficial gas velocity along the length of the adsorber.

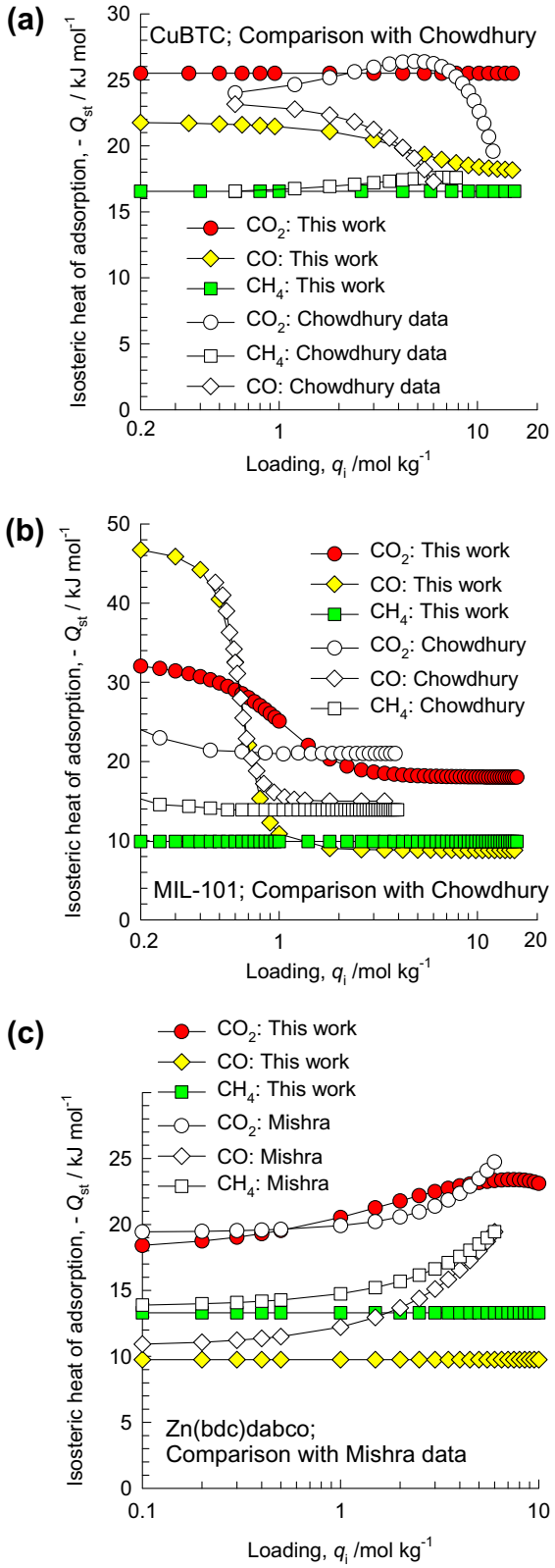

Fig. 3. The isosteric heat of adsorption for CO_2, CH_4, and CO in (a) CuBTC, (b) MIL-101, and (c) Zn(bdc)dabco at 300 K. Our calculations are compared to those presented in the works of Chowdhury et al. [21] and Mishra et al. [22].

The molar loadings of the species i, $q_i(z,t)$ at any position z, and time t are determined from IAST calculations. Eq. (3) is first subjected to finite volume discretization. Typically, the adsorber length L is divided into 100 slices. The number of slices is deter-

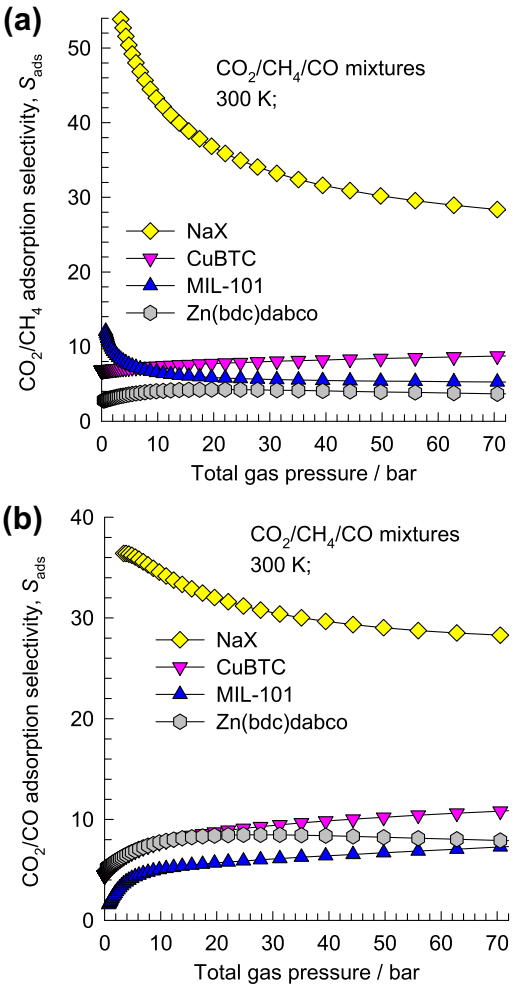

Fig. 4. Calculations of the (a) CO_2/CH_4, and (b) CO_2/CO adsorption selectivities, S_{ads}, for equimolar CO_2/CH_4/CO ternary gas mixtures at 300 K using CuBTC, MIL-101, Zn(bdc)dabco, and NaX zeolite. The calculations are based on the Ideal Adsorbed Solution Theory (IAST) using the pure component isotherm fits.

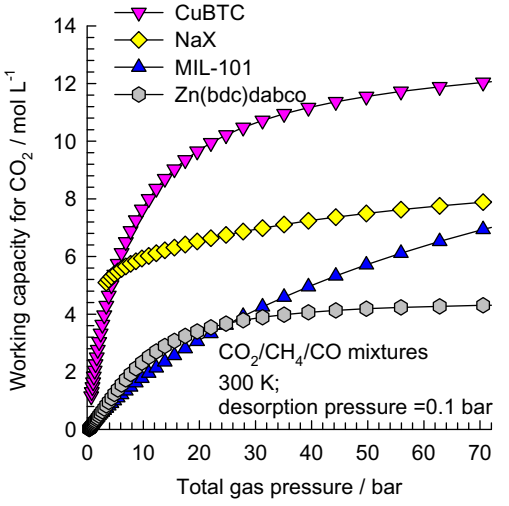

Fig. 5. Calculations of working capacities per L of adsorbent for selective adsorption of CO_2 from equimolar CO_2/CH_4/CO ternary gas mixtures at 300 K using CuBTC, MIL-101, Zn(bdc)dabco, and NaX zeolite. The calculations are based on the Ideal Adsorbed Solution Theory (IAST) using the pure component isotherm fits with parameters specified in the Supplementary material. The desorption pressure is assumed to be 0.1 bar.

mined by checking that the obtained breakthrough results do not change on increasing it. Combination of the discretized PDEs along with the algebraic IAST equilibrium model, results in a set of differential-algebraic equations (DAEs), which are solved using BESIRK [36]. BESIRK is a sparse matrix solver, based on the semi-implicit Runge–Kutta method originally developed by Michelsen [37], and extended with the Bulirsch–Stoer extrapolation method [38]. Use of BESIRK improves the numerical solution efficiency in solving the set of DAEs. The evaluation of the sparse Jacobian required in the numerical algorithm is largely based on analytic expressions [39]. Further details of the adsorber model, along with the numerical procedures used in this work, are provided in our earlier works [39–41]. Typical computation times for a binary gas mixture breakthrough are less than 100 s, allowing such transient adsorber calculations to be routinely used for screening purposes.

The solution to Eq. (3) yields $p_i(t,z)$, from which we can calculate the mol% CO_2 in the outlet gas mixture as a function of time. The comparison of the breakthrough characteristics of CuBTC, MIL-101, Zn(bdc)dabco, and NaX for $p_{10} = p_{20} = p_{30} = 10$ bar are provided in Fig. 6b.

For a specified purity of CO_2 in the outlet gas, arbitrarily chosen as 0.05 mol% CO_2, the dimensionless breakthrough times, τ_{break}, can be determined for a range of inlet total gas pressures. Fig. 6c compares the dimensionless breakthrough times, τ_{break}, for different materials. Higher values of τ_{break} are desirable because longer times will be available for uptake of CO_2 before the bed needs to be regenerated. The dimensionless breakthrough times reflect a *combination* of the two metrics: S_{ads} (Fig. 4) and working capacity (Fig. 5). We note that CuBTC and NaX have higher values of τ_{break} than Zn(bdc)dabco and MIL-101 over the entire range of pressures. We should therefore expect Zn(bdc)dabco and MIL-101 to have lower propensities to adsorb CO_2.

The economics of a PSA unit for post-combustion CO_2 capture will be dictated primarily by the amount of CO_2 uptake during the adsorption cycle, i.e. during the time interval $0–\tau_{break}$; this amount can be determined from a material balance. Fig. 7a presents a plot of the number of moles of CO_2 adsorbed during the time interval $0–\tau_{break}$. Expressed as the amount CO_2 captured per L of adsorbent, CuBTC has the highest capture capacity for pressures exceeding 10 bar. For pressures below 10 bar, NaX zeolite is the best choice of adsorbent. The data in Fig. 7a are analogous to the working capacity data presented in Fig. 5, emphasizing the important contribution of capacities in determining adsorber performance. For a given set of operating conditions, the number of moles of CO_2 captured by

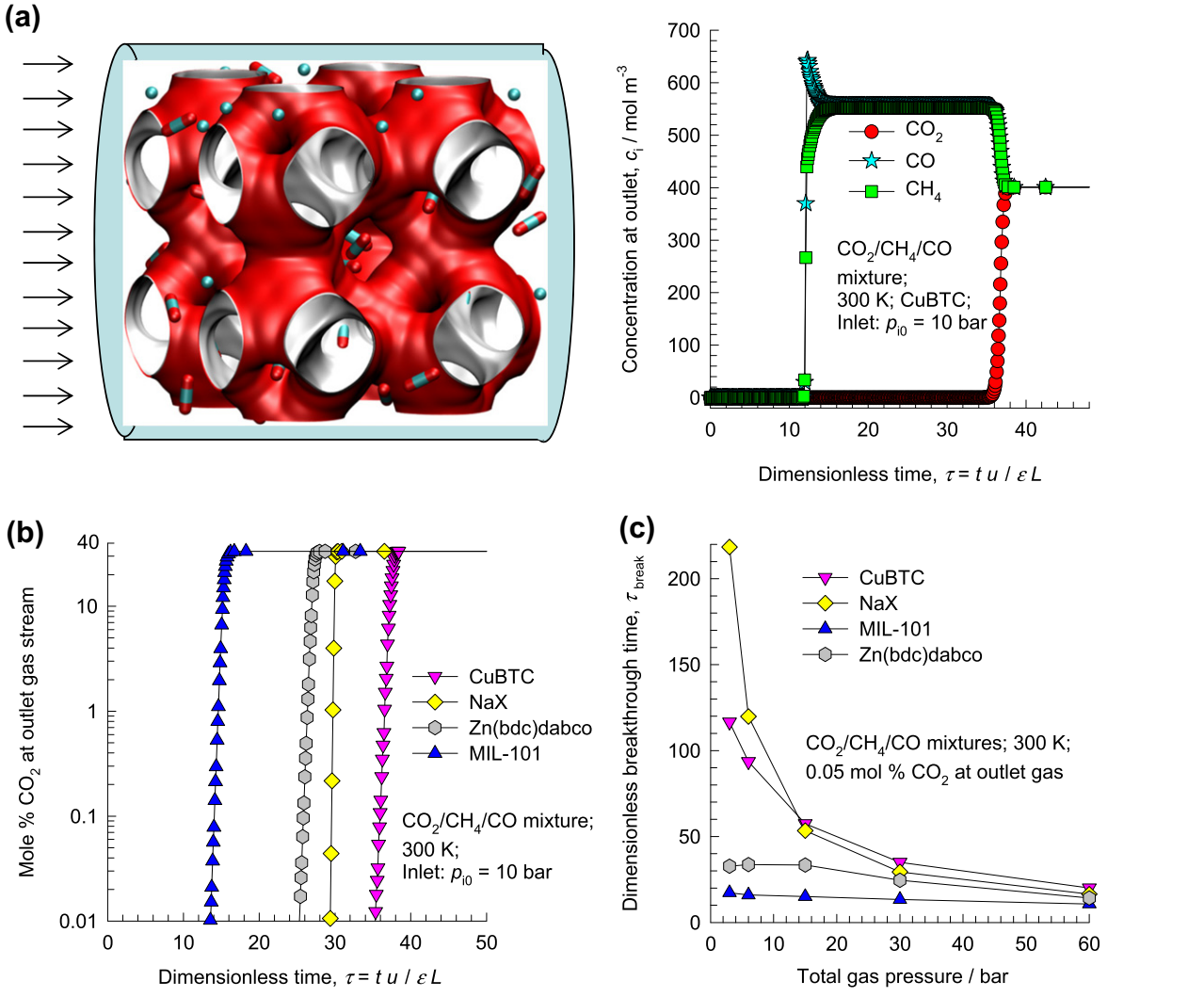

Fig. 6. (a) Transient breakthrough of equimolar $CO_2/CH_4/CO$ ternary gas mixtures ($p_{10} = p_{20} = p_{30} = 10$ bar) at 300 K using CuBTC. Specifically, the calculations presented here were performed taking the following parameter values: $L = 0.3$ m; $\varepsilon = 0.4$; $u_0 = 0.04$ m s^{-1} (at inlet). (b) Comparison of the breakthrough characteristics of CuBTC, MIL-101, Zn(bdc)dabco and NaX. (c) Comparison of the dimensionless breakthrough times, τ_{break}, for CuBTC, MIL-101, Zn(bdc)dabco, and NaX as a function of the total feed gas pressure. Video animations showing the breakthrough of a ternary gas mixture through a packed bed of CuBTC have been uploaded as Supplementary material.

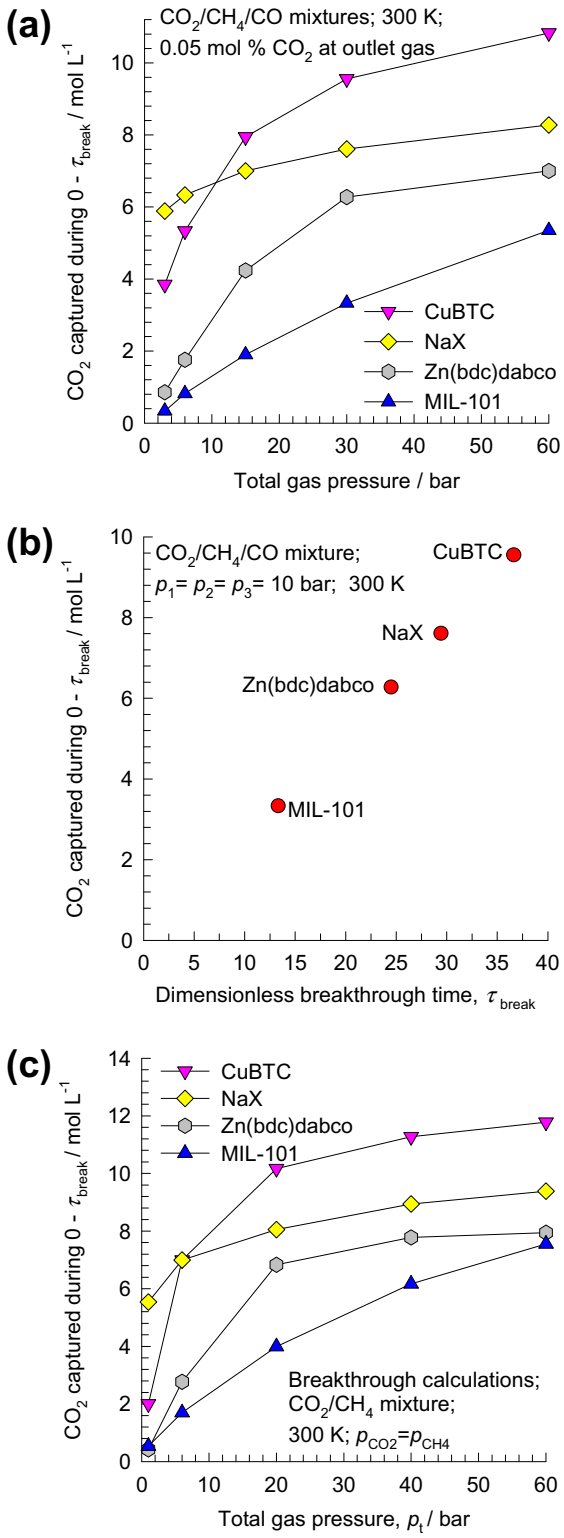

Fig. 7. (a) Comparison of the moles of CO_2 captured per L of adsorbent during the time interval $0–\tau_{break}$ for CuBTC, MIL-101, Zn(bdc)dabco, and NaX as a function of the total feed gas pressure. (b) Plot of the moles of CO_2 captured per L of adsorbent during the time interval $0–\tau_{break}$ from $CO_2/CH_4/CO$ ternary gas mixtures with CuBTC, MIL-101, Zn(bdc)dabco, and NaX as a function of the dimensionless breakthrough time, τ_{break}, for operation at 300 K with $p_{10} = p_{20} = p_{30} = 10$ bar. (c) Comparison of the moles of CO_2 captured per L of adsorbent during the time interval $0–\tau_{break}$ from CO_2/CH_4 binary gas mixtures with CuBTC, MIL-101, Zn(bdc)dabco, and NaX as a function as a function of the total feed gas pressure.

different porous materials correlates *linearly* with dimensionless breakthrough time, τ_{break}; this is illustrated in Fig. 7b for a total pressure of 30 bar. This implies that τ_{break} is the proper metric combining the selectivity and capacity metrics.

Since CO and methane breakthrough at about the same time with CuBTC (cf. Fig. 6a), this material is also the best of the four adsorbent materials considered for separation of CO_2/CO gas mixtures in absence of CH_4.

High pressure separations of CO_2/H_2, CO_2/CH_4, and $CO_2/CH_4/H_2$ mixtures have been investigated by Herm et al. [1,15]. In agreement with the conclusions we have reached in the foregoing analysis, these authors have also concluded that the low pore volume of NaX leads to severe capacity limitations in PSA operations and consequently this zeolite is not an attractive choice for use at high pressures despite having high selectivities. The best adsorbent for the three mixtures determined on the basis of breakthrough calculations was MgMOF-74, and the reasons for this can be traced to the following main factors: (a) the availability of exposed metal sites which exert orbital interactions with CO_2 guest molecules offering *selectivity*, (b) reasonably high pore volume (0.57 $cm^3\ g^{-1}$) ensuring high working *capacities* in PSA operations.

It must be emphasized here that though diffusional effects are ignored and thermodynamic equilibrium is assumed to prevail within the adsorber, the hierarchy of adsorbent materials obtained in Fig. 7b does not change if diffusional effects are considered because diffusivities in CuBTC and NaX, the two best adsorbents, are not expected to differ widely the cage sizes are comparable in size.

Furthermore, the conclusion that CuBTC is the best adsorbent is not altered if other compositions for the mixture are chosen. To confirm this we carried out CO_2/CH_4 binary mixture breakthroughs, i.e. without the presence of CO, using the same four materials for a range of operating pressures. Fig. 7c shows that the hierarchy of adsorbents is precisely the same as for the ternary gas mixtures; CuBTC is the best adsorbent for this separation task when pressures exceed 6 bar.

4. Conclusions

This work, which had the major objective of evaluating the performance of different adsorbents for separation of CO_2/CH_4/CO gas mixtures, leads to the following set of conclusions.

1) Experimental data on pure component isotherms, obtained in terms of excess loadings need to be converted to absolute loadings before fitting to models such as that of Langmuir.
2) The isosteric heats of adsorption and adsorption selectivities are properly calculated only on the basis of fits of absolute loadings.
3) The adsorption selectivity and capacity metrics do not necessarily go hand-in-hand. This leads to a dilemma in selection of adsorbents. The situation with respect to NaX zeolite is particularly noteworthy. For operations at pressures below 10 bar, NaX has the highest capture capacity per L of adsorbent material used (cf. Fig. 7a), whereas for operations exceeding 10 bar CuBTC outperforms NaX purely on capacity considerations which overcome selectivity limitations.
4) Both metrics, adsorption selectivity, S_{ads}, and the CO_2 working capacity, influence the CO_2 capture capacity in a PSA unit. The dimensionless breakthrough time, τ_{break}, reflects the right combination of the selectivity and capacity metrics that is a proper measure of the performance of PSA units. A high value of τ_{break} is desirable in practice because it reduces the frequency of required regeneration. Our studies highlight the pitfalls in using just the adsorption selectivity in choosing adsorbents; capacity factors become significant at higher pressures.

5) Of the four materials considered, CuBTC emerges as the best adsorbent for separation of $CO_2/CH_4/CO$ gas mixtures at pressures exceeding 10 bar, despite having a significantly lower selectivity compared to NaX zeolite. Before Cu-BTC can be used in separations on an industrial scale several remaining questions have to be resolved, in particular its stability toward water vapor [20]. Furthermore, heat effects and regeneration aspects need to be considered in subsequent process development activities.

Acknowledgement

The author acknowledges Dr. S. Gumma for providing the isotherm data in terms of excess loadings for purposes of re-fitting.

Appendix A. Supplementary data

Supplementary data associated with this article can be found, in the online version, at doi:10.1016/j.micromeso.2012.02.034.

References

[1] Z.R. Herm, J.A. Swisher, B. Smit, R. Krishna, J.R. Long, J. Am. Chem. Soc. 133 (2011) 5664–5667.
[2] J.A. Mason, K. Sumida, Z.R. Herm, R. Krishna, J.R. Long, Energy Environ. Sci. 3 (2011) 3030–3040.
[3] T.M. McDonald, D.M. D'Alessandro, R. Krishna, J.R. Long, Chem. Sci. 2 (2011) 2022–2028.
[4] A.Ö. Yazaydın, R.Q. Snurr, T.H. Park, K. Koh, J. Liu, M.D. LeVan, A.I. Benin, P. Jakubczak, M. Lanuza, D.B. Gallarkoway, J.J. Low, R.R. Willis, J. Am. Chem. Soc. 131 (2009) 18198–18199.
[5] R. Krishna, J.M. van Baten, J. Membr. Sci. 360 (2010) 323–333.
[6] R. Krishna, J.M. van Baten, Phys. Chem. Chem. Phys. 13 (2011) 10593–10616.
[7] M. Palomino, A. Corma, F. Rey, Langmuir 26 (2010) 1910–1917.
[8] D. Zhao, D.J. Timmons, D. Yuan, H. Zhou, Acc. Chem. Res. 44 (2011) 123–133.
[9] J. An, N.L. Rosi, J. Am. Chem. Soc. 132 (2010) 5578–5579.
[10] D. Britt, H. Furukawa, B. Wang, T.G. Glover, O.M. Yaghi, Proc. Natl. Acad. Sci. USA 106 (2009) 20637–20640.
[11] E.D. Bloch, L. Murray, W.L. Queen, S. Chavan, S.N. Maximoff, J.P. Bigi, R. Krishna, V.K. Peterson, F. Grandjean, G.J. Long, B. Smit, S. Bordiga, C.M. Brown, J.R. Long, J. Am. Chem. Soc. 133 (2011) 14814–14822.
[12] S. Couck, J.F.M. Denayer, G.V. Baron, T. Rémy, J. Gascon, F. Kapteijn, J. Am. Chem. Soc. 131 (2009) 6326–6327.
[13] J.M. Simmons, H. Wu, W. Zhou, T. Yildirim, Energy Environ. Sci. 4 (2011) 2177–2185.
[14] K. Sumida, D.L. Rogow, J.A. Mason, T.M. McDonald, E.D. Bloch, Z.R. Herm, T.-H. Bae, J.R. Long, Chem. Rev. 112 (2012) 724–781.
[15] Z.R. Herm, R. Krishna, J.R. Long, Microporous Mesoporous Mater. 151 (2012) 481–487.
[16] Y. Belmabkhout, G. Pirngruber, E. Jolimaitre, A. Methivier, Adsorption 13 (2007) 341–349.
[17] S. Wang, Q. Yang, C. Zhong, Sep. Purif. Technol. 60 (2008) 30–35.
[18] J.R. Karra, K.S. Walton, Langmuir 24 (2008) 8620–8626.
[19] J.R. Karra, K.S. Walton, J. Phys. Chem. C 114 (2010) 15735–15740.
[20] L. Hamon, E. Jolimaître, G. Pirngruber, Ind. Eng. Chem. Res. 49 (2010) 7497–7503.
[21] P. Chowdhury, S. Mekala, F. Dreisbach, S. Gumma, Microporous Mesoporous Mater. 152 (2012) 246–252.
[22] P. Mishra, S. Mekala, F. Dreisbach, B. Mandal, S. Gumma, Sep. Purif. Technol. (2012). http://www.dx.doi.org/10.1016/j.seppur.2011.09.041.
[23] K.S. Walton, M.D. LeVan, Sep. Sci. Technol. 41 (2006) 485–500.
[24] S. Cavenati, C.A. Grande, A.E. Rodrigues, J. Chem. Eng. Data 49 (2004) 1095–1101.
[25] A.L. Myers, P.A. Monson, Langmuir 18 (2002) 10261–10273.
[26] A.L. Myers, J.M. Prausnitz, AIChE J. 11 (1965) 121–130.
[27] R. Krishna, J.R. Long, J. Phys. Chem. C 115 (2011) 12941–12950.
[28] Y. He, Z. Zhang, S. Xiang, F.R. Fronczek, R. Krishna, B. Chen, Chem. Eur. J. 18 (2012) 613–619.
[29] Y. He, Z. Zhang, S. Xiang, H. Wu, F.R. Fronczek, W. Zhou, R. Krishna, M. O'Keeffe, B. Chen, Chem. Eur. J. 18 (2012) 1901–1904.
[30] J. Moellmer, A. Moeller, F. Dreisbach, R. Glaeser, R. Staudt, Microporous Mesoporous Mater. 138 (2011) 140–148.
[31] A. Bhown, M. Haranczyk, S. Kaye, J.R. Long, E. Masanet, J. Reimer, B. Smit, High-Throughput Discovery of Robust Metal–Organic Frameworks for Carbon Dioxide Capture, University of California, Berkeley. <http://www.2011showcase.lbl.gov/presentations/CarbonCapture_Smit.pdf> (accessed 20 August 2011).
[32] R. Kumar, Ind. Eng. Chem. Res. 33 (1994) 1600–1605.
[33] L. Hamon, P.L. Llewellyn, T. Devic, A. Ghoufi, G. Clet, V. Guillerm, G.D. Pirngruber, G. Maurin, C. Serre, G. Driver, W. van Beek, E. Jolimaître, A. Vimont, M. Daturi, G. Férey, J. Am. Chem. Soc. 131 (2009) 17490–17499.
[34] M.T. Ho, G.W. Allinson, D.E. Wiley, Ind. Eng. Chem. Res. 47 (2008) 4883–4890.
[35] R. Krishna, J.M. van Baten, Sep. Purif. Technol. 87 (2012) 120–126.
[36] H.A. Kooijman, R. Taylor, AIChE J. 41 (1995) 1852–1863.
[37] M. Michelsen, AIChE J. 22 (1976) 594–597.
[38] R. Bulirsch, J. Stoer, Numer. Math. 8 (1966) 1–14.
[39] R. Krishna, R. Baur, Sep. Purif. Technol. 33 (2003) 213–254.
[40] R. Krishna, J.M. van Baten, J. Membr. Sci. 377 (2011) 249–260.
[41] R. Krishna, R. Baur, Diffusion, Adsorption and Reaction in Zeolites: Modelling and Numerical Issues, University of Amsterdam, Amsterdam, <http://www.science.uva.nl/research/cr/zeolite/> (accessed 8 March 2011).

Supplementary Material to accompany:

Adsorptive separation of $CO_2/CH_4/CO$ gas mixtures at high pressures

Rajamani Krishna*

Van 't Hoff Institute for Molecular Sciences, University of Amsterdam, Science Park 904,

1098 XH Amsterdam, The Netherlands

*Corresponding author: Tel +31 20 6270990; Fax: + 31 20 5255604; email: r.krishna@uva.nl

1. Structural details of microporous materials

Three different MOFs: CuBTC, MIL-101, Zn(bdc)dabco, along with NaX zeolite have been evaluated for the separation of mixtures containing CO_2, CH_4, and CO.

The pore landscapes of CuBTC, MIL-101, Zn(bdc)dabco, and NaX zeolite are presented in Figures 1, 2, 3, and 4.

The pore volumes are as follows:

CuBTC: 0.75 $cm^3\ g^{-1}$; this is the measured pore volume reported by Chowdhury et al.[1]

MIL-101: 1.38 $cm^3\ g^{-1}$; this is the measured pore volume obtained by N_2 adsorption in the experiments of Lebedev et al.[2]

NaX: 0.28 $cm^3\ g^{-1}$; this is the measured pore volume in the experiments of Belmabkhout et al.[3]

Zn(bdc)dabco: 0.67 $cm^3\ g^{-1}$; this is the measured pore volume obtained in the experiments of Mishra al.[4]

The framework densities are as follows:

CuBTC: 879 kg m^{-3} = 0.879 kg L^{-1}

MIL-101: 440 kg m^{-3} = 0.44 kg L^{-1}

NaX: 1421 kg m^{-3} = 1.421 kg L^{-1}

Zn(bdc)dabco: 826 kg m^{-3} = 0.826 kg L^{-1}

2. Dual-site Langmuir fits of pure component isotherms in CuBTC and MIL-101

The measured experimental data on excess loadings published by Chowdhury et al. [1] on pure component isotherms for CO_2, CH_4, and CO at 295 K, 318 K, and 353 K in CuBTC and MIL-101 were first converted to absolute loadings using the Peng-Robinson equation of state for estimation of the fluid phase molar densities within the pores.

The pure component isotherm data for CO_2, CH_4, and CO, expressed in terms of absolute loadings, were fitted with the dual-site Langmuir isotherm model

$$q \equiv q_A + q_B = \frac{q_{sat,A} b_A p}{1 + b_A p} + \frac{q_{sat,B} b_B p}{1 + b_B p} \tag{1}$$

where the temperature dependences of the Langmuir constants are expressed as

$$b_A = b_{A0} \exp\left(\frac{E_A}{RT}\right); \quad b_B = b_{B0} \exp\left(\frac{E_B}{RT}\right) \tag{2}$$

For CO_2/CuBTC, CH_4/CuBTC and CH_4/MIL-101, the 1-site Langmuir model was sufficiently accurate. The saturation capacities $q_{i,sat}$, Langmuir constants b_i, for the two sites, A, and B, are provided in Tables 1, 2, 3, 4, 5, and 6. Figures 5, 6 7, 8, 9, and 10 compare the absolute component loadings with the dual-site Langmuir fits. The dual-site Langmuir model provides an excellent representation of all six guest-host combinations.

3. Absolute vs Excess loadings

For a clear exposition of the fundamental definitions of absolute and excess loadings in microporous materials, the reader is referred to the recent paper by Gumma and Talu [5].

Plotted in Figures 5, 6 7, 8, 9, and 10 are the original excess loadings data of Chowdhury et al. [1]. For all six guest-host combinations, the differences between absolute and excess loadings are significant for pressures exceeding about 10 bar. In the paper by Chowdhury et al. [1] the isotherms fits were based on excess loadings. Their approach is fundamentally flawed. This is because excess loadings often exhibit a maximum in the loadings at extremely high pressures; such a maximum is not amenable to fitting by thermodynamically consistent models such as that due to Langmuir. Isotherm fitting with models such as Langmuir and Toth should be done using absolute loadings; this has been pointed out by Myers and Monson [6]. In order to illustrate the maximum in the excess loading isotherm data, Figure 11 presents the published high pressure experimental data of Getzschmann et al.[7] for adsorption of CH_4 in CuBTC.

The estimation of the absolute loadings requires good estimates of the pore volume. In order to investigate the sensitivity of the results to uncertainties in the pore volume, Figure 12 compares the absolute loading for CH_4 in CuBTC at 295 K, calculated for pore volumes of 0.70 cm^3/g, 0.75 cm^3/g, and 0.80 cm^3/g. The results are practically indistinguishable from one another. Uncertainties in the estimation of the pore volume should not deter researchers from correcting the excess loadings to obtain absolute loadings for fitting purposes.

A further point to note is that the differences between absolute and excess loadings is higher for components with lower adsorption strength. This is most evident by the data for CH_4 and CO adsorption in CuBTC and MIL-101. At the highest pressures the absolute loadings of these guest molecules in MIL-101 are 55% higher than the corresponding excess loadings. As illustration, Figure 13 compares absolute and excess loadings for adsorption of CH_4 in (a) CuBTC, and (b) MIL-101 at 295 K. The absolute and excess loadings are plotted in these diagrams. The continuous solid lines represent the fits of the absolute loadings from this work. The dashed lines are the fits of Chowdhury et al.[1] for the excess loadings. Figures 14a, and 14b provide the corresponding comparisons for adsorption of CO. Due to the significantly larger pore volume of MIL-101, the differences between absolute and excess loadings are significant over a much wider range of pressures than for CuBTC.

4. Dual-site Langmuir fits of pure component isotherms in NaX zeolite

For evaluating the performance of NaX zeolite in separation of $CO_2/CH_4/CO$ gas mixtures we used the pure component experimental data of Belmabkhout et al.[3] and Cavenati et al.[8] for adsorption of CO_2, CH_4, and CO at a variety of temperatures. The excess loading reported in these papers are converted to absolute loadings using a pore volume of 0.28 cm^3/g, along with the Peng-Robinson equation of state for estimation of the fluid phase densities within the pores. The dual-site Langmuir model was used for fitting purposes. The fitted parameters are specified in Tables 7, 8, and 9.

5. Fits of pure component isotherms in Zn(bdco)dabco

For evaluating the performance of Zn(bdc)dabco in separation of $CO_2/CH_4/CO$ gas mixtures we used the pure component experimental data of Mishra et al.[4]. These data were measured to pressure ranging to 27 bar, and temperatures of 284 K, 314 K, and 350 K. Mishra et al.[4] have fitted their isotherm data in terms of excess loadings. For the reasons outline in the foregoing discussions, we need to re-fit the isotherms after conversion to absolute loadings. The excess loading reported in these papers are converted to absolute loadings using a pore volume of 0.67 cm^3/g, along with the Peng-Robinson equation of state for estimation of the fluid phase densities within the pores. For CH_4 and CO adsorption, a simple 1-site Langmuir was found to be sufficiently accurate to describe the absolute loadings for all three temperatures 284 K, 314 K, and 350 K for the entire pressure range. The fitting of CO_2 isotherm data is somewhat more complicated, and requires a 2-site Langmuir-Freundlich model:

$$q_i = q_{i,A,sat}\frac{b_{i,A}p_i^{\nu_{i,A}}}{1+b_{i,A}p_i^{\nu_{i,A}}} + q_{i,B,sat}\frac{b_{i,B}p_i^{\nu_{i,B}}}{1+b_{i,B}p_i^{\nu_{i,B}}} \qquad (3)$$

The fit parameters are specified in Tables 10, 11, and 12.

6. Isosteric heat of adsorption

The isosteric heat of adsorption, Q_{st}, defined as

$$Q_{st} = -RT^2\left(\frac{\partial \ln p}{\partial T}\right)_q \qquad (4)$$

were determined using the pure component isotherm fits. Figures 15a, 16a, 17, and 18 present the data on the isosteric heat of adsorption for CO_2, CH_4, and CO in, respectively, CuBTC, MIL-101, NaX, and Zn(bdc)dabco. These calculations are based on the use of equation (4), along with analytic differentiation of the isotherm fits of the dual-Langmuir fit constants provided in Tables 1, 2, 3, 4, 5, and 6. The analytic procedure used is identical to the one described in detail in the Supplementary Information accompanying the paper by Mason et al.[9]

The derivative in equation (4) is obtained with the *absolute* loading, q, held constant; see Myers and Monson [6]. In the work of Chowdhury et al. [1] and Mishra et al. [4],, the isosteric heats are calculated using fits of excess loadings. Consequently, by implication, their values are obtained with derivatives in which the *excess loadings* are held constant. Their calculated values of the isosteric heats of adsorption are expected to be different to those obtained in this work. Figures 15b, and 16b compare the calculations of the isosteric heats of adsorption for CuBTC and MIL-101 obtained in this work, with those reported by Chowdhury et al. [1]. There are significant differences in the two sets of values for both MOFs. For CuBTC the differences are apparent only at higher loadings. For MIL-101, there are significant differences over the entire range of loadings. The reason for this can be traced to the significantly higher pore volume for MIL-101 which results in a significantly large difference between excess and absolute loadings over a wide range of operating pressures.

Figure 18 presents the isosteric heats of adsorption for CO_2, CH_4, and CO in Zn(bdc)dabco. Our calculations compared to those presented in the work of Mishra et al. [4]. While the two sets of calculations are reasonably close at low loadings, there are significant deviations at higher loadings for CH_4 and CO for which the differences between absolute and excess loadings are large.

7. IAST calculations of selectivity and capacity for separation of $CO_2/CH_4/CO$ gas mixtures

Using the pure component isotherm fits, the adsorption selectivities defined by

$$S_{ads} = \frac{q_1/q_2}{p_1/p_2} \tag{5}$$

can be determined using the Ideal Adsorbed Solution Theory (IAST) of Myers and Prausnitz.[10] The accuracy of IAST for estimation of binary mixture equilibrium in zeolites and MOFs has been established in a number of publications in the literature [11-14].

Figure 19 shows the IAST calculations of the adsorption selectivity, S_{ads}, for a ternary $CO_2/CH_4/CO$ equimolar (i.e. $p_1 = p_2 = p_3$) gas mixtures at 300 K in CuBTC, MIL-101, Zn(bdc)dabco, and NaX. Figure 19a shows the CO_2/CH_4 adsorption selectivity. Figure 19b shows the CO_2/CO adsorption

selectivity. In both cases, NaX zeolite is found to have the highest selectivities over the entire range of pressures.

The performance of a PSA unit is dictated not only by adsorption selectivity but also by the working capacity, as has been emphasized in several publications [9, 15-21]. Let us define the working capacity for selective adsorption of CO_2 from $CO_2/CH_4/CO$ gas mixtures as the component loading of CO_2 in the mixture at the operating pressure minus that at a desorption pressure of 0.1 bar. The working capacity can be expressed in the usual manner as mol per kg of adsorbent. Alternatively, the working capacity can be expressed as mol per L of adsorbent. For converting one capacity measure to the author we need the framework densities.

Figures 20a, and 20b compare the working capacities for CuBTC, MIL-101, Zn(bdc)dabco, and NaX. With increasing pressures, the working capacity of NaX tends to reach plateau values, because saturation conditions are reached. This is because of the relatively low pore volume of Nax (0.28 cm^3/g) compared to the much higher pore volumes of CuBTC (0.75 cm^3/g), and MIL-101 (1.38 cm^3/g). It is interesting to note that MIL-101 that has the most "open" structure, the working capacity in terms of mol/kg is highest for operations at pressures exceeding 60 bar.

The information presented in Figures 19, and 20 underline the dilemma faced in adsorbent selection. NaX has the best selectivities, but is limited by capacity considerations for operation at pressures exceeding 1 bar. In order to resolve this dilemma we need to consider the breakthrough characteristics in a packed bed adsorber.

8. Simulations of breakthrough in a packed bed adsorber

The appropriate combination of the selectivity and capacity characteristics is reflected in the breakthrough behaviors in a packed bed adsorber. Figure 21 shows a schematic of a packed bed adsorber.

The breakthrough calculations were performed using the methodology described in the paper by Krishna and Long [20]. Assuming plug flow of $CO_2/CH_4/CO$ gas mixture through a fixed bed maintained under isothermal conditions and negligible pressure drop, the partial pressures in the gas

phase at any position and instant of time are obtained by solving the following set of partial differential equations for each of the species *i* in the gas mixture.

$$\frac{1}{RT}\varepsilon\frac{\partial p_i(t,z)}{\partial t} = -\frac{1}{RT}\frac{\partial\left(u(t,z)p_i(t,z)\right)}{\partial z} - (1-\varepsilon)\rho\frac{\partial q_i(t,z)}{\partial t}; \quad i = 1,2,3 \tag{6}$$

In equation (6), t is the time, z is the distance along the adsorber, ρ is the framework density, ε is the bed voidage, and u is the superficial gas velocity.

The adsorber bed is initially free of adsorbates, i.e. we have the initial condition

$$t = 0; \quad q_i(0,z) = 0 \tag{7}$$

At time, t = 0, the inlet to the adsorber, z = 0, is subjected to a step input of the ternary gas mixture and this step input is maintained till the end of the adsorption cycle when steady-state conditions are reached.

$$t \geq 0; \quad p_i(0,t) = p_{i0}; \quad u(0,t) = u_0 \tag{8}$$

where u_0 is the superficial gas velocity at the inlet to the adsorber.

Invoking the constraint of negligible pressure drop, the overall material balance is obtained by summing equation (6) over the three species

$$\frac{1}{RT}p_t\frac{\partial\left(u(t,z)\right)}{\partial z} = -(1-\varepsilon)\rho\sum_{i=1}^{3}\frac{\partial q_i(t,z)}{\partial t} \tag{9}$$

Equation (9) allows the calculation of the superficial gas velocity along the length of the adsorber. The molar loadings of the species *i*, q_i, at any position z, and time t are determined from IAST calculations. Details of the numerical procedures used are available in earlier works [20, 22, 23]. Specifically, the calculations presented here were performed taking the following parameter values: L = 0.3 m; ε = 0.4; u_0= 0.04 m/s (at inlet).When comparing different materials, the fractional voidage is held constant at ε = 0.4. This implies the volume of adsorbents used are the same for CuBTC, MIL-101, Zn(bdc)dabco, and NaX. The total mass of the adsorbents used is governed by the framework density.

Breakthrough calculations were performed for equimolar $CO_2/CH_4/CO$ ternary gas mixtures at 300 K using. The inlet gas was maintained at partial pressures $p_{10} = p_{20} = p_{30}$. As illustration, Figure 22 shows the outlet gas compositions as a function of the *dimensionless* time, τ, obtained by dividing the actual time, t, by the contact time between the gas and the crystallites, $\varepsilon L/u$. For a given adsorbent, under chosen operating conditions, the breakthrough characteristics are uniquely defined by τ, allowing the results to be presented here to be equally applicable to laboratory scale equipment as well as to industrial scale adsorbers.

From the information presented in Figure 22, we can calculate the mole % CO_2 in the outlet gas mixture. The comparison of the breakthrough characteristics of CuBTC, MIL-101, Zn(bdc)dabco, and NaX for $p_{10} = p_{20} = p_{30} = 10$ bar are provided in Figure 23.

Figure 24 presents a comparison of the superficial gas velocity at the outlet of the adsorber packed with CuBTC, MIL-101, Zn(bdc)dabco and NaX for $p_{10} = p_{20} = p_{30} = 10$ bar. The data show that the gas velocity changes with time, and is properly accounted for in the breakthrough calculations.

For a specified purity of CO_2 in the outlet gas, arbitrarily chosen as 0.05 mole % CO_2, the dimensionless breakthrough times, τ_{break}, can be determined for a range of inlet total gas pressures. Figure 25 compares the dimensionless breakthrough times, τ_{break}, for CuBTC, MIL-101, Zn(bdc)dabco, and NaX. Higher values of τ_{break} are desirable because longer times will be available for uptake of CO_2 before the bed needs to be regenerated. The dimensionless breakthrough times reflect a *combination* of the two metrics: S_{ads} (Figure 19) and working capacity (Figure 20). We note that CuBTC and NaX have higher values of τ_{break} than MIL-101 over the entire range of pressures. We should therefore expect MIL-101 to have poor propensities to adsorb CO_2.

The economics of a PSA unit for post-combustion CO_2 capture will be dictated primarily by the amount of CO_2 uptake during the adsorption cycle, i.e. during the time interval $0 - \tau_{break}$; this amount can be determined from a material balance. Figure 26 presents a plot of the number of moles of CO_2 adsorbed during the time interval $0 - \tau_{break}$ for CuBTC, MIL-101, Zn(bdc)dabco, and NaX as a function

of the total feed gas pressure. In Figure 26a the amount adsorbed is mole CO_2 per kg of adsorbent. In Figure 26b the amount adsorbed is mole CO_2 per L of adsorbent.

Expressed as the amount CO_2 adsorbed per kg of adsorbent, CuBTC has the highest uptake capacity over the entire pressure range. Expressed as the amount CO_2 adsorbed per L of adsorbent, NaX has the highest uptake capacity for total gas pressures below 10 bar., whereas above 10 bar, CuBTC is superior to NaX.

Acknowledgements

The author acknowledges Dr. S. Gumma for providing the isotherm data in terms of excess loadings for purposes of re-fitting.

9. Notation

$b_{i,A}$	dual-Langmuir-Freundlich constant for species *i* at adsorption site A, $Pa^{-\nu_i}$
$b_{i,B}$	dual-Langmuir-Freundlich constant for species *i* at adsorption site B, $Pa^{-\nu_i}$
L	length of packed bed adsorber, m
p_i	partial pressure of species *i* in mixture, Pa
p_t	total system pressure, Pa
q_i	component molar loading of species *i*, mol kg^{-1}
Q_{st}	isosteric heat of adsorption, J mol^{-1}
R	gas constant, 8.314 J mol^{-1} K^{-1}
S_{ads}	adsorption selectivity, dimensionless
t	time, s
T	absolute temperature, K
u	superficial gas velocity entering the packed bed, m s^{-1}
z	distance along the adsorber, m

Greek letters

ε	voidage of packed bed, dimensionless
ν	exponent in dual-Langmuir-Freundlich isotherm, dimensionless
ρ	framework density, kg m^{-3}
τ	time, dimensionless
τ_{break}	breakthrough time, dimensionless

Subscripts

i	referring to component *i*
t	referring to total mixture
A	referring to site A
B	referring to site B

10. References

[1] P. Chowdhury, S. Mekala, F. Dreisbach, S. Gumma, Adsorption of CO, CO_2 and CH_4 on Cu-BTC and MIL-101 Metal Organic Frameworks: Effect of Open Metal Sites and Adsorbate Polarity, Microporous Mesoporous Mater. 152 (2012) 246-252.

[2] O.I. Lebedev, F. Millange, C. Serre, G. Van Tendeloo, G. Férey, First Direct Imaging of Giant Pores of the Metal−Organic Framework MIL-101, Chem. Mater. 17 (2005) 6525-6527.

[3] Y. Belmabkhout, G. Pirngruber, E. Jolimaitre, A. Methivier, A complete experimental approach for synthesis gas separation studies using static gravimetric and column breakthrough experiments, Adsorption 13 (2007) 341-349.

[4] P. Mishra, S. Mekala, F. Dreisbach, B. Mandal, S. Gumma, Adsorption of CO_2, CO, CH_4 and N_2 on a zinc based metal organic framework, Sep. Purif. Technol. XX (2012) XXX-XXX. (http://dx.doi.org/10.1016/j.seppur.2011.09.041)

[5] S. Gumma, O. Talu, Net Adsorption: A Thermodynamic Framework for Supercritical Gas Adsorption and Storage in Porous Solids, Langmuir 26 (2010) 17013-17023.

[6] A.L. Myers, P.A. Monson, Adsorption in Porous Materials at High Pressure: Theory and Experiment, Langmuir 18 (2002) 10261-10273.

[7] J. Getzschmann, I. Senkovska, D. Wallacher, M. Tovar, D. Fairen-Jimenez, T. Düren, J.M. van Baten, R. Krishna, S. Kaskel, Methane storage mechanism in the Metal-Organic Framework $Cu_3(btc)_2$: An *in situ* neutron diffraction study, Microporous Mesoporous Mater. 136 (2010) 50-58.

[8] S. Cavenati, C.A. Grande, A.E. Rodrigues, Adsorption Equilibrium of Methane, Carbon Dioxide, and Nitrogen on Zeolite 13X at High Pressures, J. Chem. Eng. Data 49 (2004) 1095-1101.

[9] J.A. Mason, K. Sumida, Z.R. Herm, R. Krishna, J.R. Long, Evaluating Metal-Organic Frameworks for Post-Combustion Carbon Dioxide Capture via Temperature Swing Adsorption, Energy Environ. Sci. 3 (2011) 3030-3040.

[10] A.L. Myers, J.M. Prausnitz, Thermodynamics of mixed gas adsorption, A.I.Ch.E.J. 11 (1965) 121-130.

[11] R. Krishna, S. Calero, B. Smit, Investigation of Entropy effects during Sorption of Mixtures of Alkanes in MFI zeolite, Chem. Eng. J. 88 (2002) 81-94.

[12] R. Krishna, J.M. van Baten, Using molecular simulations for screening of zeolites for separation of CO_2/CH_4 mixtures, Chem. Eng. J. 133 (2007) 121-131.

[13] R. Krishna, J.M. van Baten, In silico screening of metal-organic frameworks in separation applications, Phys. Chem. Chem. Phys. 13 (2011) 10593-10616.

[14] R. Krishna, J.M. van Baten, Investigating the potential of MgMOF-74 membranes for CO_2 capture, J. Membr. Sci. 377 (2011) 249-260.

[15] R. Kumar, Pressure Swing Adsorption Process: Performance Optimum and Adsorbent Selection, Ind. Eng. Chem. Res. 33 (1994) 1600-1605.

[16] L. Hamon, P.L. Llewellyn, T. Devic, A. Ghoufi, G. Clet, V. Guillerm, G.D. Pirngruber, G. Maurin, C. Serre, G. Driver, W. van Beek, E. Jolimaître, A. Vimont, M. Daturi, G. Férey, Co-adsorption and Separation of CO_2-CH_4 Mixtures in the Highly Flexible MIL-53(Cr) MOF, J. Am. Chem. Soc. 131 (2009) 17490-17499.

[17] M.T. Ho, G.W. Allinson, D.E. Wiley, Reducing the Cost of CO_2 Capture from Flue Gases Using Pressure Swing Adsorption, Ind. Eng. Chem. Res. 47 (2008) 4883-4890.

[18] Z.R. Herm, R. Krishna, J.R. Long, CO_2/CH_4, CH_4/H_2 and $CO_2/CH_4/H_2$ separations at high pressures using Mg2(dobdc), Microporous Mesoporous Mater. 151 (2012) 481-487.

[19] Z.R. Herm, J.A. Swisher, B. Smit, R. Krishna, J.R. Long, Metal-Organic Frameworks as Adsorbents for Hydrogen Purification and Pre-Combustion Carbon Dioxide Capture J. Am. Chem. Soc. 133 (2011) 5664-5667.
[20] R. Krishna, J.R. Long, Screening metal-organic frameworks by analysis of transient breakthrough of gas mixtures in a fixed bed adsorber, J. Phys. Chem. C 115 (2011) 12941-12950.
[21] R. Krishna, J.M. van Baten, A comparison of the CO_2 capture characteristics of zeolites and metal-organic frameworks, Sep. Purif. Technol. 87 (2012) 120-126.
[22] K.S. Walton, M.D. LeVan, Consistency of Energy and Material Balances for Bidisperse Particles in Fixed-Bed Adsorption and Related Applications, Ind. Eng. Chem. Res. 42 (2003) 6938-6948.
[23] R. Krishna, R. Baur, Modelling issues in zeolite based separation processes, Sep. Purif. Technol. 33 (2003) 213-254.

Table 1. 1-site Langmuir parameters for pure CO_2 isotherms in CuBTC.

$$q = \frac{q_{sat} bp}{1 + bp}$$

$$q_{sat} = 18.2 \,\mathrm{mol\,kg^{-1}}$$

$$b = b_0 \exp\left(\frac{E}{RT}\right);$$

$$b_0 = 1.37 \times 10^{-10} \ \mathrm{Pa^{-1}}$$

$$E = 25.5 \ \mathrm{kJ\ mol^{-1}}$$

Table 2. 1-site Langmuir parameters for pure CH_4 isotherms in CuBTC.

$$q = \frac{q_{sat} bp}{1 + bp}$$

$$q_{sat} = 15.9 \,\mathrm{mol\,kg^{-1}}$$

$$b = b_0 \exp\left(\frac{E}{RT}\right);$$

$$b_0 = 8.34 \times 10^{-10} \ \mathrm{Pa^{-1}}$$

$$E = 16.55 \ \mathrm{kJ\ mol^{-1}}$$

Table 3. Dual-site Langmuir parameters for pure CO isotherms in CuBTC.

$$q \equiv q_A + q_B = \frac{q_{sat,A} b_A p}{1 + b_A p} + \frac{q_{sat,B} b_B p}{1 + b_B p}$$

$q_{sat,A} = 3.8 \,\text{mol kg}^{-1}$

$q_{sat,B} = 11.6 \,\text{mol kg}^{-1}$

$$b_A = b_{A0} \exp\left(\frac{E_A}{RT}\right);$$

$b_{A0} = 3.08 \times 10^{-10}$ Pa^{-1}

$E_A = 23$ kJ mol^{-1}

$$b_B = b_{B0} \exp\left(\frac{E_B}{RT}\right);$$

$b_{B0} = 2.3 \times 10^{-10}$ Pa^{-1}

$E_B = 18$ kJ mol^{-1}

Table 4. Dual-site Langmuir parameters for pure CO_2 isotherms in MIL-101.

$$q \equiv q_A + q_B = \frac{q_{sat,A} b_A p}{1 + b_A p} + \frac{q_{sat,B} b_B p}{1 + b_B p}$$

$q_{sat,A} = 1 \text{ mol kg}^{-1}$

$q_{sat,B} = 45 \text{ mol kg}^{-1}$

$$b_A = b_{A0} \exp\left(\frac{E_A}{RT}\right);$$

$b_{A0} = 3.31 \times 10^{-11} \text{ Pa}^{-1}$

$E_A = 36 \text{ kJ mol}^{-1}$

$$b_B = b_{B0} \exp\left(\frac{E_B}{RT}\right);$$

$b_{B0} = 1.98 \times 10^{-10} \text{ Pa}^{-1}$

$E_B = 18 \text{ kJ mol}^{-1}$

Table 5. 1-site Langmuir parameters for pure CH_4 isotherms in MIL-101.

$$q = \frac{q_{sat} bp}{1 + bp}$$

$$q_{sat} = 34 \,\mathrm{mol\,kg^{-1}}$$

$$b = b_0 \exp\left(\frac{E}{RT}\right);$$

$$b_0 = 1.79 \times 10^{-9} \ \mathrm{Pa^{-1}}$$

$$E = 9.9 \ \mathrm{kJ\ mol^{-1}}$$

Table 6. Dual-site Langmuir parameters for pure CO isotherms in MIL-101.

$$q \equiv q_A + q_B = \frac{q_{sat,A} b_A p}{1 + b_A p} + \frac{q_{sat,B} b_B p}{1 + b_B p}$$

$q_{sat,A} = 0.65 \,\text{mol kg}^{-1}$

$q_{sat,B} = 24.2 \,\text{mol kg}^{-1}$

$$b_A = b_{A0} \exp\left(\frac{E_A}{RT}\right);$$

$b_{A0} = 7.27 \times 10^{-13}$ Pa^{-1}

$E_A = 48.2$ kJ mol^{-1}

$$b_B = b_{B0} \exp\left(\frac{E_B}{RT}\right);$$

$b_{B0} = 12.71 \times 10^{-9}$ Pa^{-1}

$E_B = 8.8$ kJ mol^{-1}

Table 7. Dual-site Langmuir parameter for adsorption of CO_2 in NaX zeolite. These parameters were determined by fitting adsorption isotherm data reported in the works of Belmabkhout et al.[3] and Cavenati et al.[8], after converting the reported excess isotherm data to absolute loadings.

$$q \equiv q_A + q_B = \frac{q_{sat,A} b_A p}{1 + b_A p} + \frac{q_{sat,B} b_B p}{1 + b_B p}$$

$q_{sat,A} = 3.5\,\text{mol kg}^{-1}$

$q_{sat,B} = 5.2\,\text{mol kg}^{-1}$

$$b_A = b_{A0} \exp\left(\frac{E_A}{RT}\right);$$

$b_{A0} = 3.64 \times 10^{-13}\ \text{Pa}^{-1}$

$E_A = 35\ \text{kJ mol}^{-1}$

$$b_B = b_{B0} \exp\left(\frac{E_B}{RT}\right);$$

$b_{B0} = 6.04 \times 10^{-11}\ \text{Pa}^{-1}$

$E_B = 35\ \text{kJ mol}^{-1}$

Table 8. Dual-site Langmuir parameter for adsorption of CH_4 in NaX zeolite. These parameters were determined by fitting adsorption isotherm data reported in the work of Belmabkhout et al.[3], after converting the reported excess isotherm data to absolute loadings.

$$q \equiv q_A + q_B = \frac{q_{sat,A} b_A p}{1 + b_A p} + \frac{q_{sat,B} b_B p}{1 + b_B p}$$

$q_{sat,A} = 4 \text{ mol kg}^{-1}$

$q_{sat,B} = 5 \text{ mol kg}^{-1}$

$$b_A = b_{A0} \exp\left(\frac{E_A}{RT}\right);$$

$b_{A0} = 3.66 \times 10^{-10} \text{ Pa}^{-1}$

$E_A = 14 \text{ kJ mol}^{-1}$

$$b_B = b_{B0} \exp\left(\frac{E_B}{RT}\right);$$

$b_{B0} = 3.75 \times 10^{-9} \text{ Pa}^{-1}$

$E_B = 14 \text{ kJ mol}^{-1}$

Table 9. Dual-site Langmuir parameter for adsorption of CO in NaX zeolite. These parameters were determined by fitting adsorption isotherm data reported in the work of Belmabkhout et al.[3], after converting the reported excess isotherm data to absolute loadings.

$$q \equiv q_A + q_B = \frac{q_{sat,A} b_A p}{1 + b_A p} + \frac{q_{sat,B} b_B p}{1 + b_B p}$$

$q_{sat,A} = 4.5 \text{ mol kg}^{-1}$

$q_{sat,B} = 3.5 \text{ mol kg}^{-1}$

$$b_A = b_{A0} \exp\left(\frac{E_A}{RT}\right);$$

$b_{A0} = 3.15 \times 10^{-11} \text{ Pa}^{-1}$

$E_A = 20.5 \text{ kJ mol}^{-1}$

$$b_B = b_{B0} \exp\left(\frac{E_B}{RT}\right);$$

$b_{B0} = 1.11 \times 10^{-9} \text{ Pa}^{-1}$

$E_B = 20.5 \text{ kJ mol}^{-1}$

Table 10. Dual-site Langmuir-Freundlich parameter for adsorption of CO_2 in Zn(bdc)dabco.

$$q = q_{A,sat}\frac{b_A p^{\nu_A}}{1+b_A p^{\nu_A}} + q_{i,B,sat}\frac{b_B p^{\nu_B}}{1+b_B p^{\nu_B}}$$

$q_{sat,A} = 6 \text{ mol kg}^{-1}$

$q_{sat,B} = 8 \text{ mol kg}^{-1}$

$b_A = b_{A0}\exp\left(\frac{E_A}{RT}\right);$

$b_{A0} = 1.8\times10^{-9} \text{ Pa}^{-1}$

$E_A = 18 \text{ kJ mol}^{-1}$

$\nu_A = 1$

$b_B = b_{B0}\exp\left(\frac{E_B}{RT}\right);$

$b_{B0} = 1.45\times10^{-19} \text{ Pa}^{-\nu B}$

$E_B = 48 \text{ kJ mol}^{-1}$

$\nu_B = 1.88$

Table 11. 1-site Langmuir parameters for pure CH_4 isotherms in Zn(bdc)dabco.

$$q = \frac{q_{sat} bp}{1 + bp}$$

$$q_{sat} = 22 \ \text{mol kg}^{-1}$$

$$b = b_0 \exp\left(\frac{E}{RT}\right);$$

$$b_0 = 1.21 \times 10^{-9} \ \text{Pa}^{-1}$$

$$E = 13.3 \ \text{kJ mol}^{-1}$$

Table 12. 1-site Langmuir parameters for pure CO isotherms in Zn(bdc)dabco.

$$q = \frac{q_{sat} bp}{1 + bp}$$

$$q_{sat} = 18.9 \,\mathrm{mol\,kg^{-1}}$$

$$b = b_0 \exp\left(\frac{E}{RT}\right);$$

$$b_0 = 3.13 \times 10^{-10}\ \mathrm{Pa^{-1}}$$

$$E = 9.75\ \mathrm{kJ\ mol^{-1}}$$

11. Captions for Figures

Figure 1. Pore landscapes of CuBTC.

Figure 2. Pore landscapes of MIL-101.

Figure 3. Pore landscape of Zn(bdc)dabco.

Figure 4. Pore landscapes of NaX zeolite.

Figure 5. The pure component isotherm data for CO_2 in CuBTC at 295 K, 318 K, and 353 K, in terms of both absolute and excess molar loadings. The continuous solid lines are the dual-Langmuir fits using the parameters specified in Table 1. The fits are for the absolute loadings. In (a), the *x*-axis is plotted on a logarithmic scale, and in (b) the *x*-axis is on a linear scale.

Figure 6. The pure component isotherm data for CH_4 in CuBTC at 295 K, 318 K, and 353 K, in terms of both absolute and excess molar loadings. The continuous solid lines are the dual-Langmuir fits using the parameters specified in Table 2. The fits are for the absolute loadings. The fits are for the absolute loadings. In (a), the *x*-axis is plotted on a logarithmic scale, and in (b) the *x*-axis is on a linear scale.

Figure 7. The pure component isotherm data for CO in CuBTC at 295 K, 318 K, and 353 K, in terms of both absolute and excess molar loadings. The continuous solid lines are the dual-Langmuir fits using the

parameters specified in Table 3. The fits are for the absolute loadings. The fits are for the absolute loadings. In (a), the *x*-axis is plotted on a logarithmic scale, and in (b) the *x*-axis is on a linear scale.

Figure 8. The pure component isotherm data for CO_2 in MIL-101 at 295 K, 318 K, and 353 K, in terms of both absolute and excess molar loadings. The continuous solid lines are the dual-Langmuir fits using the parameters specified in Table 4. The fits are for the absolute loadings. The fits are for the absolute loadings. In (a), the *x*-axis is plotted on a logarithmic scale, and in (b) the *x*-axis is on a linear scale.

Figure 9. The pure component isotherm data for CH_4 in MIL-101 at 295 K, 318 K, and 353 K, in terms of both absolute and excess molar loadings. The continuous solid lines are the dual-Langmuir fits using the parameters specified in Table 5. The fits are for the absolute loadings. The fits are for the absolute loadings. In (a), the *x*-axis is plotted on a logarithmic scale, and in (b) the *x*-axis is on a linear scale.

Figure 10. The pure component isotherm data for CO in MIL-101 at 295 K, 318 K, and 353 K, in terms of both absolute and excess molar loadings. The continuous solid lines are the dual-Langmuir fits using the parameters specified in Table 6. The fits are for the absolute loadings. In (a), the *x*-axis is plotted on a logarithmic scale, and in (b) the *x*-axis is on a linear scale.

Figure 11. High pressure experimental data of Getzschmann et al.[7] for adsorption of CH_4 in CuBTC.

Figure 12. The absolute loading for CH_4 in CuBTC at 295 K, calculated for pore volumes of 0.70 cm^3/g, 0.75 cm^3/g, and 0.80 cm^3/g.

Figure 13. Pure component isotherm data for CH_4 in (a) CuBTC, and (b) MIL-101 at 295 K. The absolute and excess loadings are plotted in these diagrams. The continuous solid lines represent the fits of the absolute loadings from this work. The dashed lines are the fits of Chowdhury et al.[1] for the excess loadings.

Figure 14. Pure component isotherm data for CO in (a) CuBTC, and (b) MIL-101 at 295 K. The absolute and excess loadings are plotted in these diagrams. The continuous solid lines represent the fits of the absolute loadings from this work. The dashed lines are the fits of Chowdhury et al.[1] for the excess loadings.

Figure 15. The isosteric heat of adsorption for CO_2, CH_4, and CO in CuBTC. Our calculations compared to those presented in the work of Chowdhury et al.[1]. It is to be noted that the x-axis for our calculations are absolute loading, whereas for the calculations of Chowdhury et al.[1], the x-axis represents the excess loadings.

Figure 16. The isosteric heat of adsorption for CO_2, CH_4, and CO in MIL-101. Our calculations compared to those presented in the work of Chowdhury et al.[1]. It is to be noted that the x-axis for our calculations are absolute loading, whereas for the calculations of Chowdhury et al.[1], the x-axis represents the excess loadings.

Figure 17. The isosteric heat of adsorption for CO_2, CH_4, and CO in NaX zeolite.

Figure 18. The isosteric heat of adsorption for CO_2, CH_4, and CO in Zn(bdc)dabco. Our calculations compared to those presented in the work of Mishra et al. [4]. It is to be noted that the x-axis for our calculations are absolute loading, whereas for the calculations of Mishra et al. [4], the x-axis represents the excess loadings.

Figure 19. Calculations of the (a) CO_2/CH_4, and CO_2/CO adsorption selectivities, S_{ads}, for equimolar $CO_2/CH_4/CO$ ternary gas mixtures at 300 K using CuBTC, MIL-101, Zn(bdc)dabco, and NaX zeolite. The calculations are based on the Ideal Adsorbed Solution Theory (IAST) using the pure component isotherm fits.

Figure 20. Calculations of working capacities for selective adsorption of CO_2 from equimolar $CO_2/CH_4/CO$ ternary gas mixtures at 300 K using CuBTC, MIL-101, Zn(bdc)dabco, and NaX zeolite. The calculations are based on the Ideal Adsorbed Solution Theory (IAST) using the pure component isotherm fits.

Figure 21. Schematic of packed bed adsorber.

Figure 22. Transient breakthrough of equimolar $CO_2/CH_4/CO$ ternary gas mixtures at 300 K using (a) CuBTC, (b) MIL-101, (c) Zn(bdc)dabco, and (d) NaX zeolite. The inlet gas is maintained at partial pressures $p_{10} = p_{20} = p_{30} = 10$ bar.

Figure 23. Comparison of the breakthrough characteristics of CuBTC, MIL-101, Zn(bdc)dabco and NaX for $p_{10} = p_{20} = p_{30} = 10$ bar. The *y*-axis is the mole % CO_2 in the outlet gas mixture. The *x*-axis is the dimensionless breakthrough time, τ.

Figure 24. Comparison of the superficial gas velocity at the outlet of the adsorber packed with CuBTC, MIL-101, Zn(bdc)dabco and NaX for $p_{10} = p_{20} = p_{30} = 10$ bar. The *y*-axis is superficial gas velocity of the outlet gas mixture. The *x*-axis is the dimensionless breakthrough time, τ.

Figure 25. Comparison of the dimensionless breakthrough times, τ_{break}, for CuBTC, MIL-101, Zn(bdc)dabco, and NaX as a function of the total feed gas pressure.

Figure 26. Mole of CO_2 adsorbed during the time interval 0 – τ_{break} for CuBTC, MIL-101, Zn(bdc)dabco, and NaX as a function of the total feed gas pressure. In (a) the amount adsorbed is mole CO_2 per kg of adsorbent. In (b) the amount adsorbed is mole CO_2 per L of adsorbent.

Figure 1

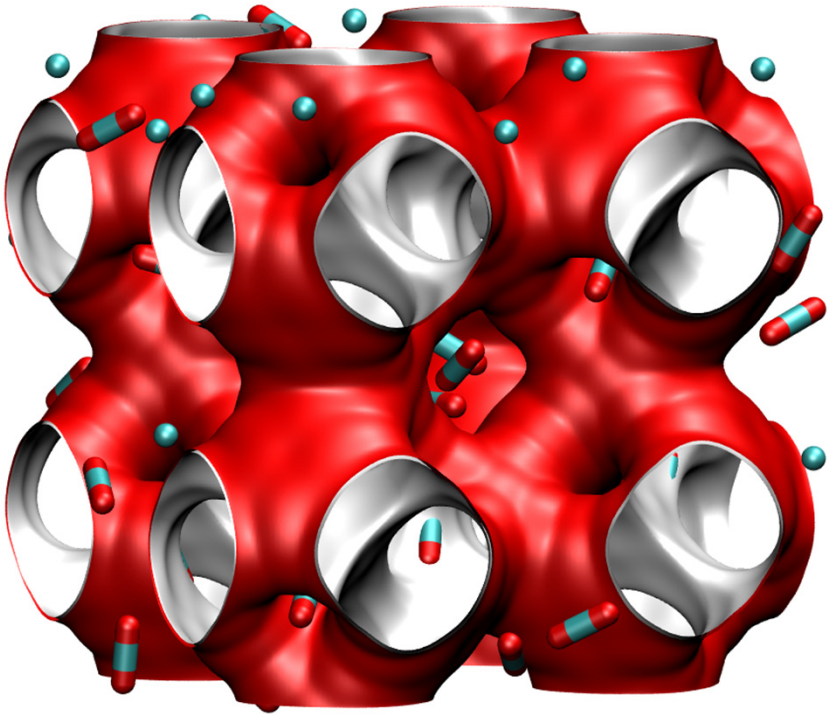

Figure 2

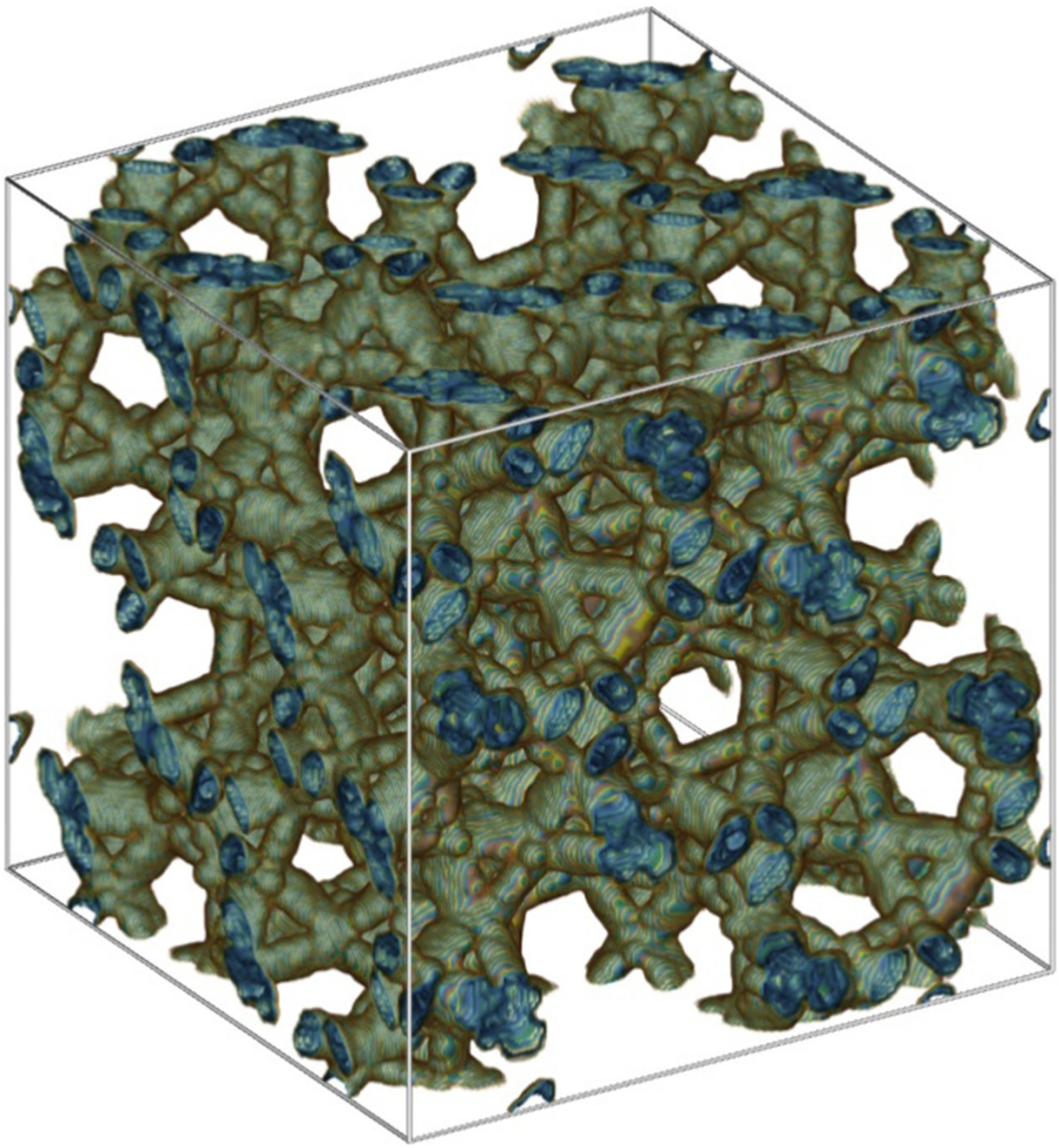

Figure 3

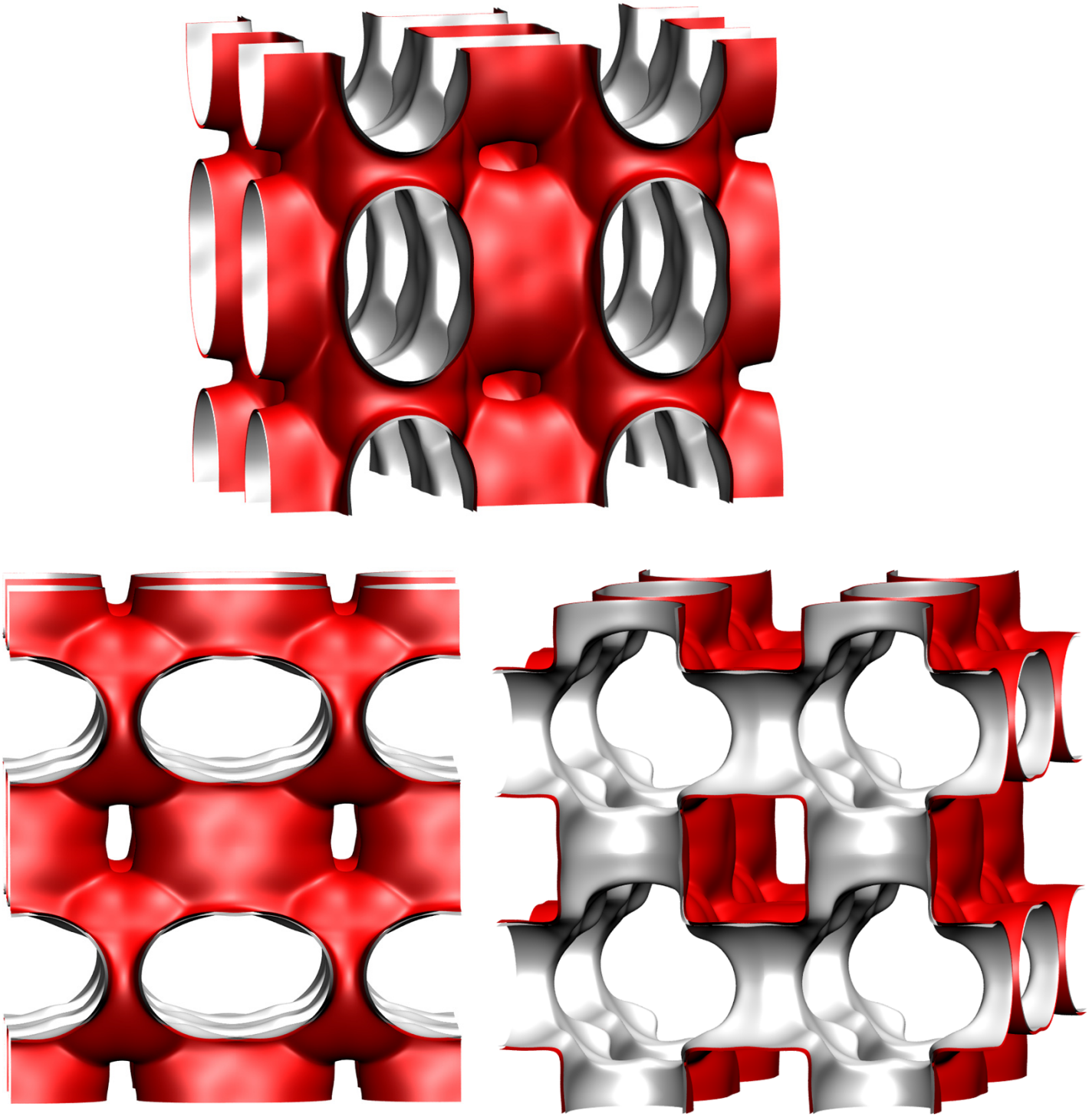

Figure 4

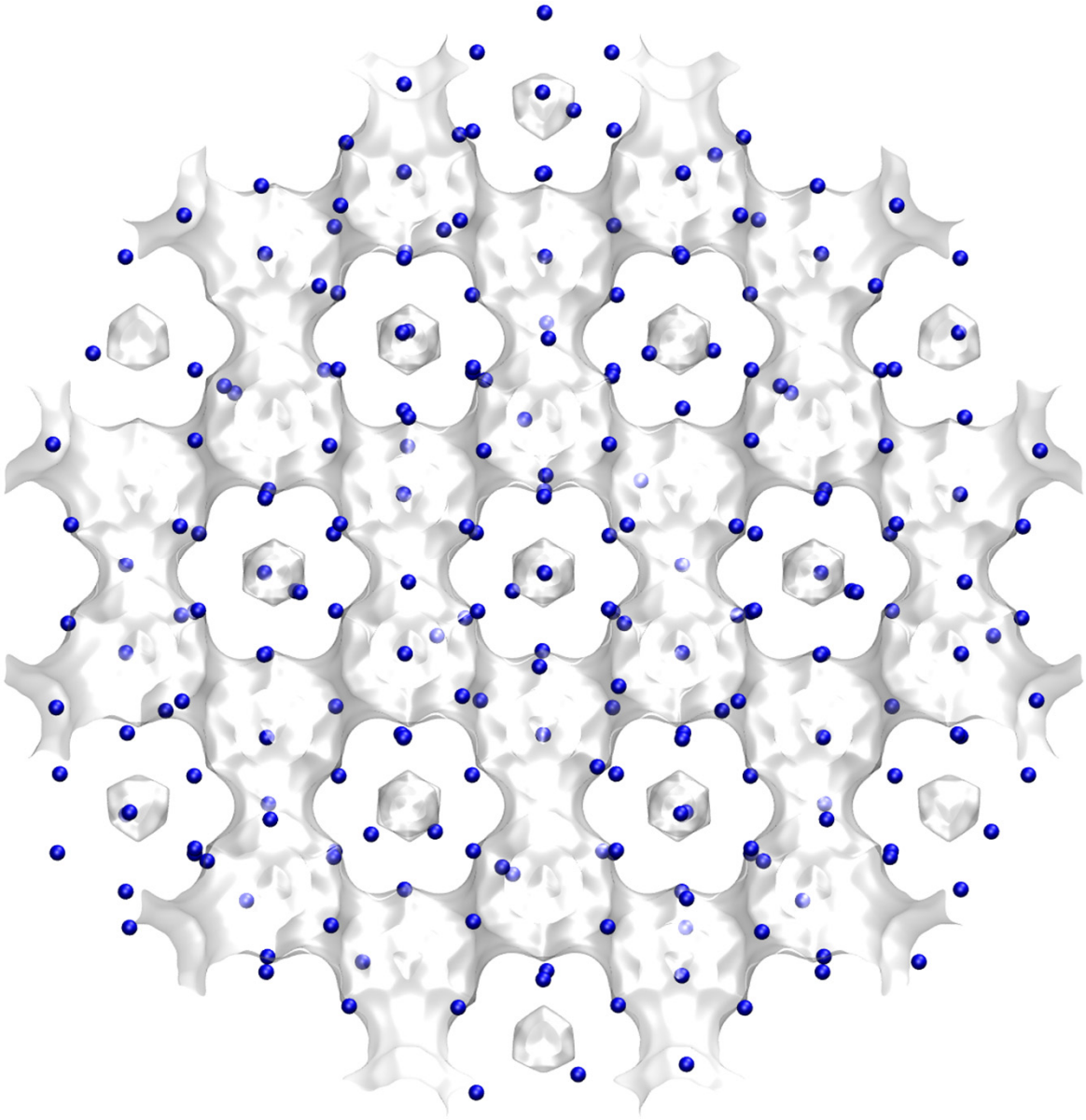

Blue spheres are cations

Figure 5

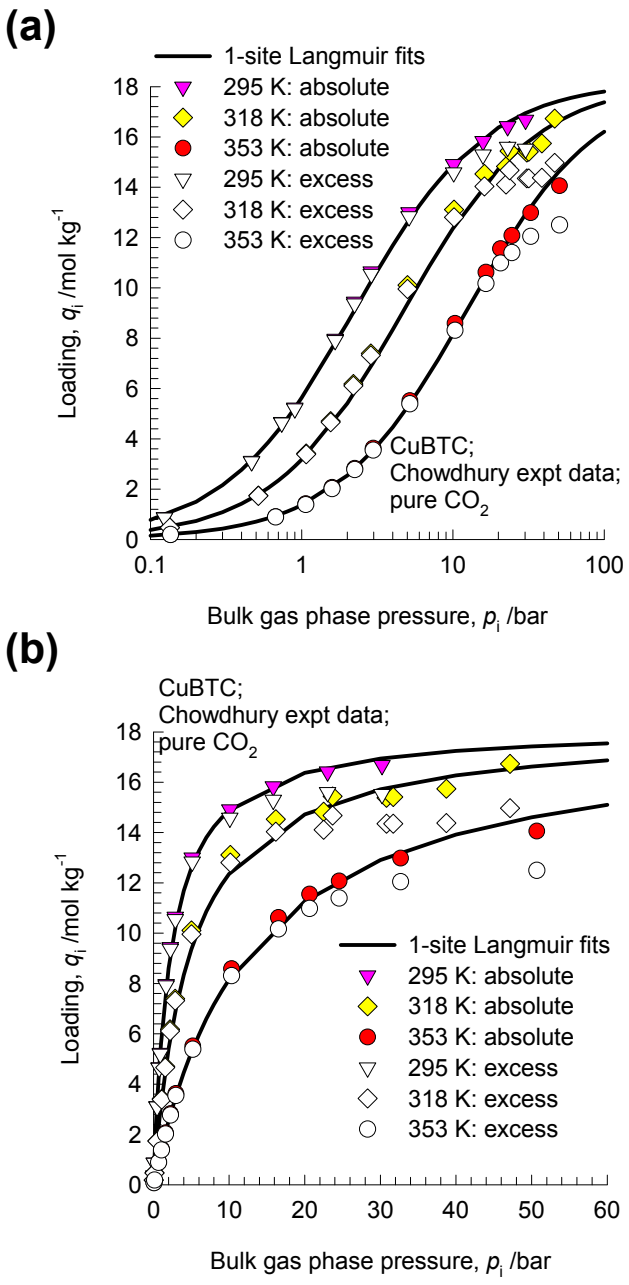
(a)
1-site Langmuir fits
295 K: absolute
318 K: absolute
353 K: absolute
295 K: excess
318 K: excess
353 K: excess
CuBTC;
Chowdhury expt data;
pure CO2
Loading, qi /mol kg-1
Bulk gas phase pressure, pi /bar
(b)
CuBTC;
Chowdhury expt data;
pure CO2
1-site Langmuir fits
295 K: absolute
318 K: absolute
353 K: absolute
295 K: excess
318 K: excess
353 K: excess
Loading, qi /mol kg-1
Bulk gas phase pressure, pi /bar

Figure 6

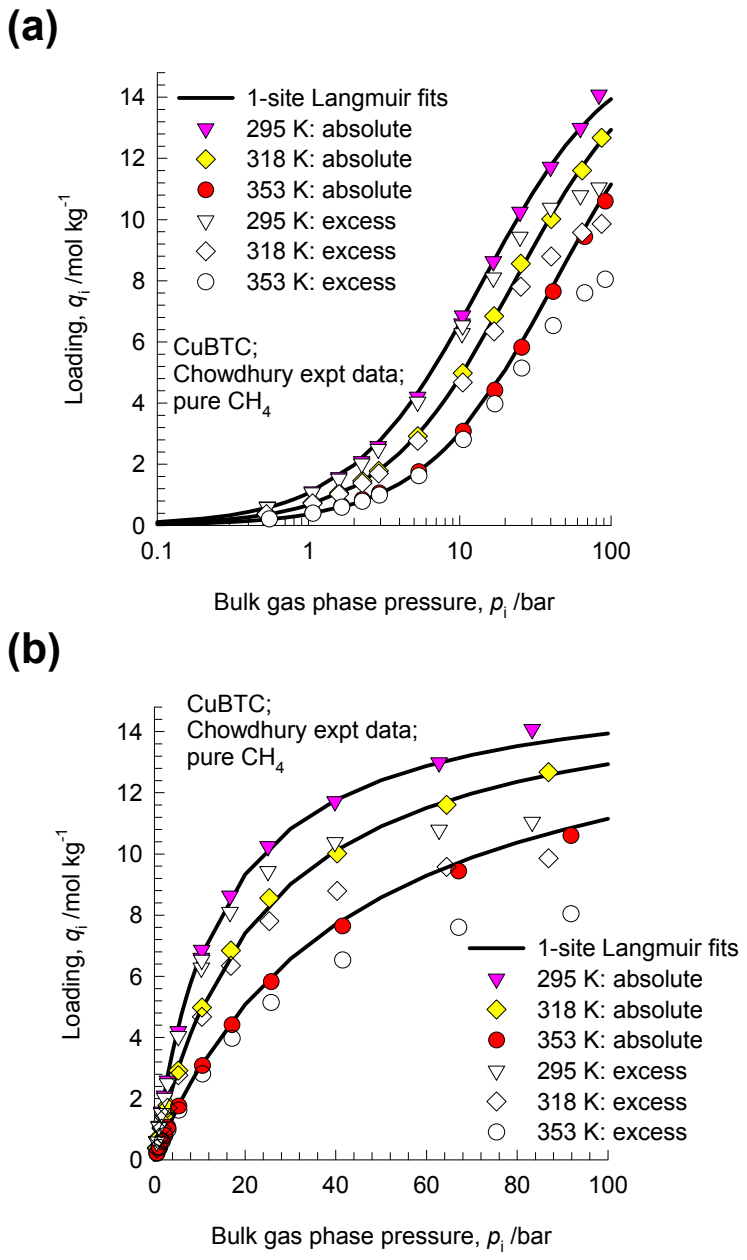
(a)
1-site Langmuir fits
295 K: absolute
318 K: absolute
353 K: absolute
295 K: excess
318 K: excess
353 K: excess
CuBTC;
Chowdhury expt data;
pure CH4
Loading, qi /mol kg-1
Bulk gas phase pressure, pi /bar
(b)
CuBTC;
Chowdhury expt data;
pure CH4
1-site Langmuir fits
295 K: absolute
318 K: absolute
353 K: absolute
295 K: excess
318 K: excess
353 K: excess
Loading, qi /mol kg-1
Bulk gas phase pressure, pi /bar

Figure 7

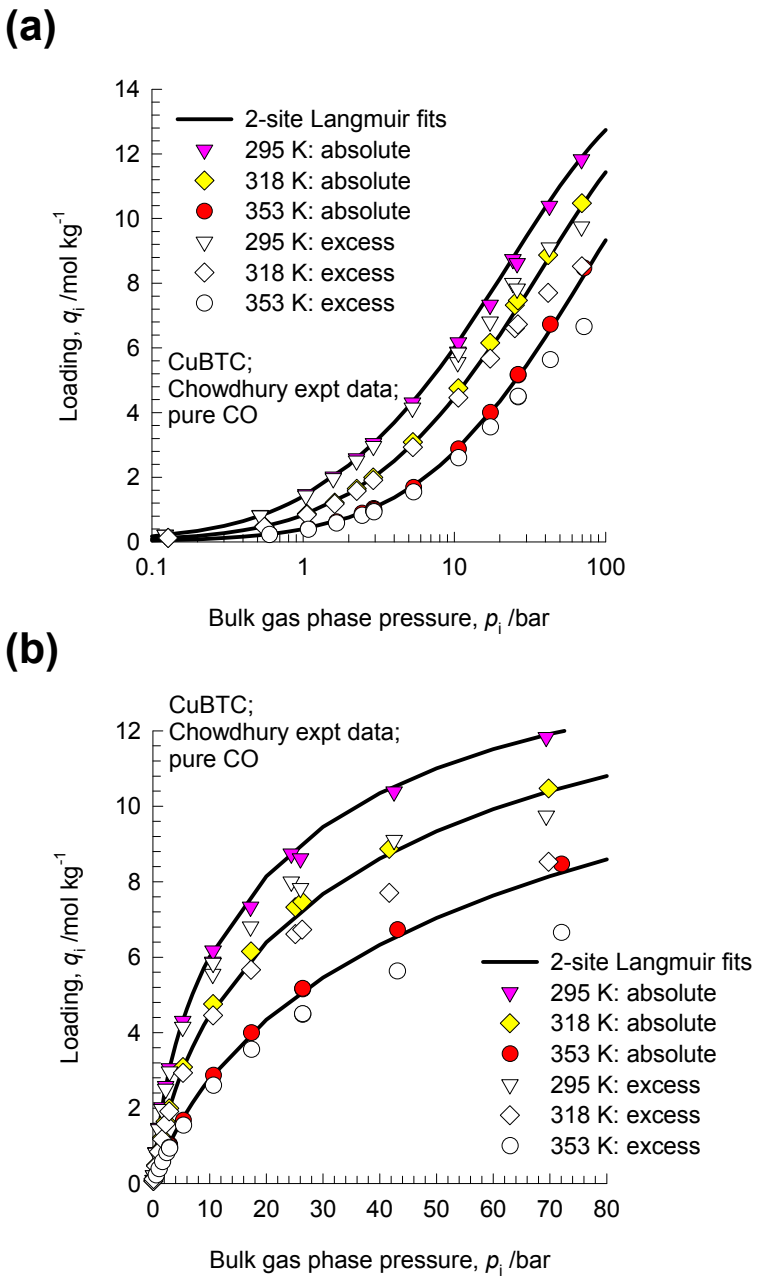
(a)
2-site Langmuir fits
295 K: absolute
318 K: absolute
353 K: absolute
295 K: excess
318 K: excess
353 K: excess
CuBTC;
Chowdhury expt data;
pure CO
Loading, q_i /mol kg^{-1}
Bulk gas phase pressure, p_i /bar
(b)
CuBTC;
Chowdhury expt data;
pure CO
2-site Langmuir fits
295 K: absolute
318 K: absolute
353 K: absolute
295 K: excess
318 K: excess
353 K: excess
Loading, q_i /mol kg^{-1}
Bulk gas phase pressure, p_i /bar

Figure 8

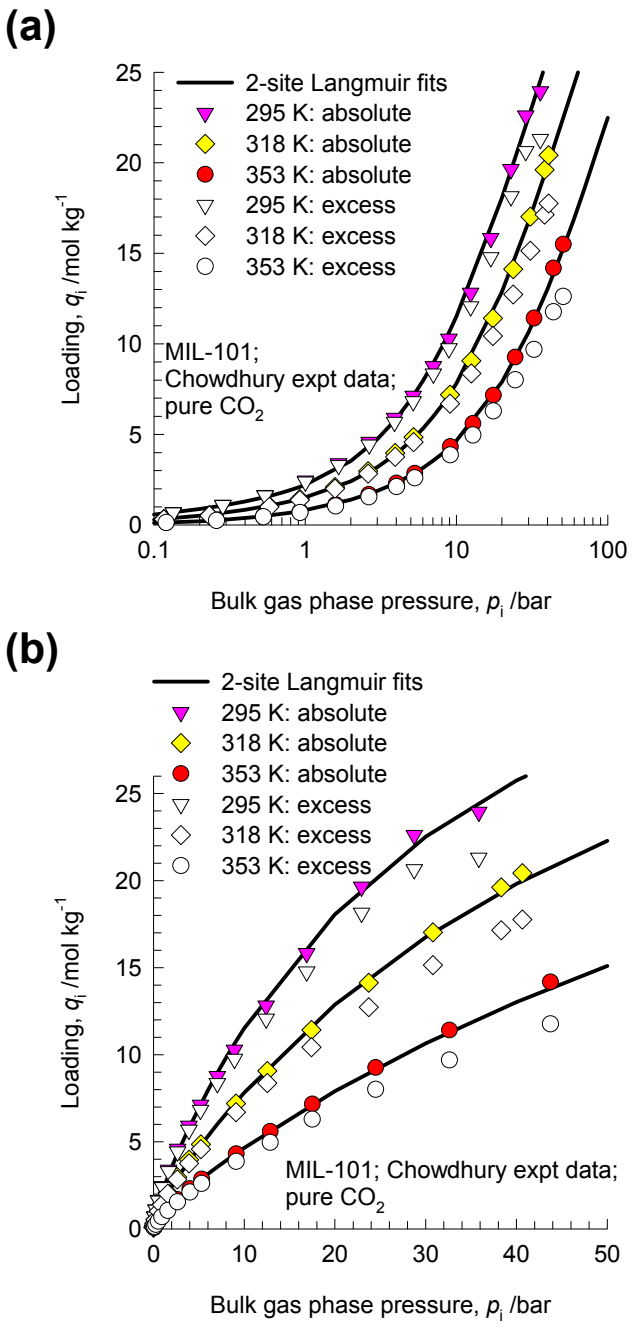
(a)
2-site Langmuir fits
295 K: absolute
318 K: absolute
353 K: absolute
295 K: excess
318 K: excess
353 K: excess
MIL-101;
Chowdhury expt data;
pure CO2
Loading, qi /mol kg-1
Bulk gas phase pressure, pi /bar
(b)
2-site Langmuir fits
295 K: absolute
318 K: absolute
353 K: absolute
295 K: excess
318 K: excess
353 K: excess
MIL-101; Chowdhury expt data;
pure CO2
Loading, qi /mol kg-1
Bulk gas phase pressure, pi /bar

Figure 9

(a)

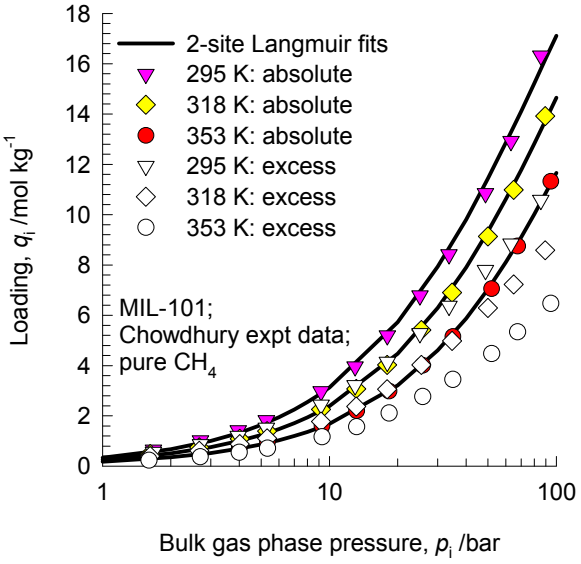
2-site Langmuir fits
295 K: absolute
318 K: absolute
353 K: absolute
295 K: excess
318 K: excess
353 K: excess
MIL-101;
Chowdhury expt data;
pure CH4
Loading, qi /mol kg-1
Bulk gas phase pressure, pi /bar
0
2
4
6
8
10
12
14
16
18
1
10
100

(b)

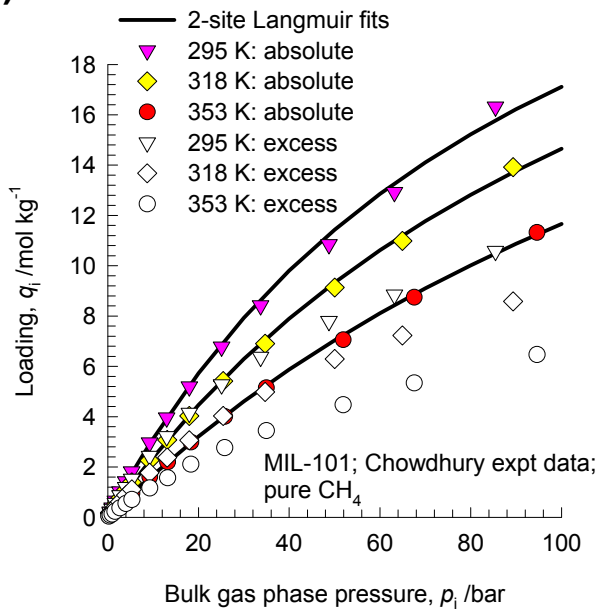
2-site Langmuir fits
295 K: absolute
318 K: absolute
353 K: absolute
295 K: excess
318 K: excess
353 K: excess
MIL-101; Chowdhury expt data;
pure CH4
Loading, qi /mol kg-1
Bulk gas phase pressure, pi /bar
0
2
4
6
8
10
12
14
16
18
0
20
40
60
80
100

Figure 10

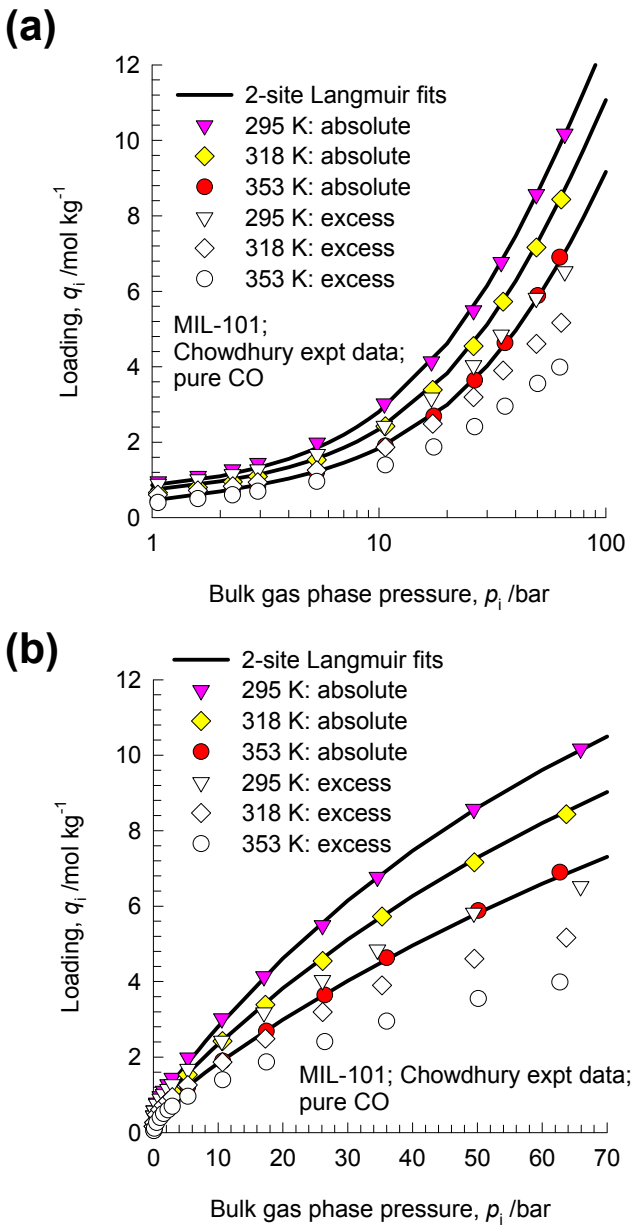
(a)
2-site Langmuir fits
295 K: absolute
318 K: absolute
353 K: absolute
295 K: excess
318 K: excess
353 K: excess
MIL-101;
Chowdhury expt data;
pure CO
Loading, q_i /mol kg^{-1}
Bulk gas phase pressure, p_i /bar
(b)
2-site Langmuir fits
295 K: absolute
318 K: absolute
353 K: absolute
295 K: excess
318 K: excess
353 K: excess
MIL-101; Chowdhury expt data;
pure CO
Loading, q_i /mol kg^{-1}
Bulk gas phase pressure, p_i /bar

Figure 11

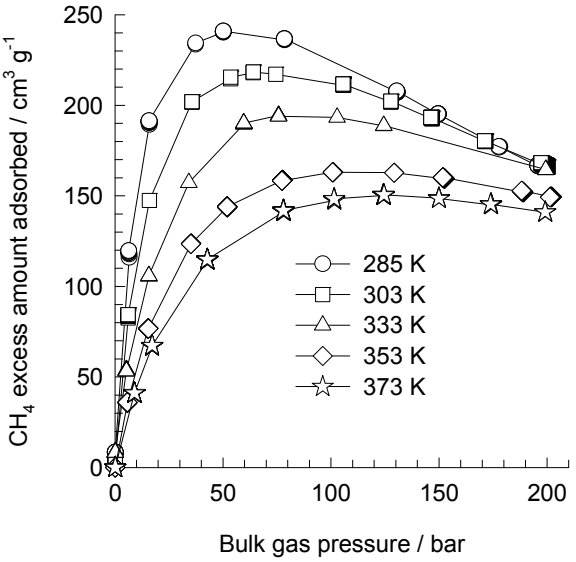
250
200
150
100
50
0
0
50
100
150
200
CH4 excess amount adsorbed / cm3 g-1
Bulk gas pressure / bar
285 K
303 K
333 K
353 K
373 K

Figure 12

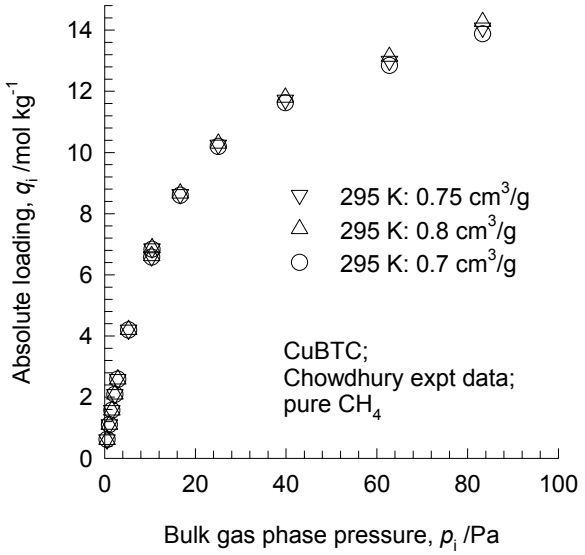
Absolute loading, q_i /mol kg^{-1}
Bulk gas phase pressure, p_i /Pa
0
2
4
6
8
10
12
14
0
20
40
60
80
100
295 K: 0.75 cm^3/g
295 K: 0.8 cm^3/g
295 K: 0.7 cm^3/g
CuBTC;
Chowdhury expt data;
pure CH$_4$

Figure 13

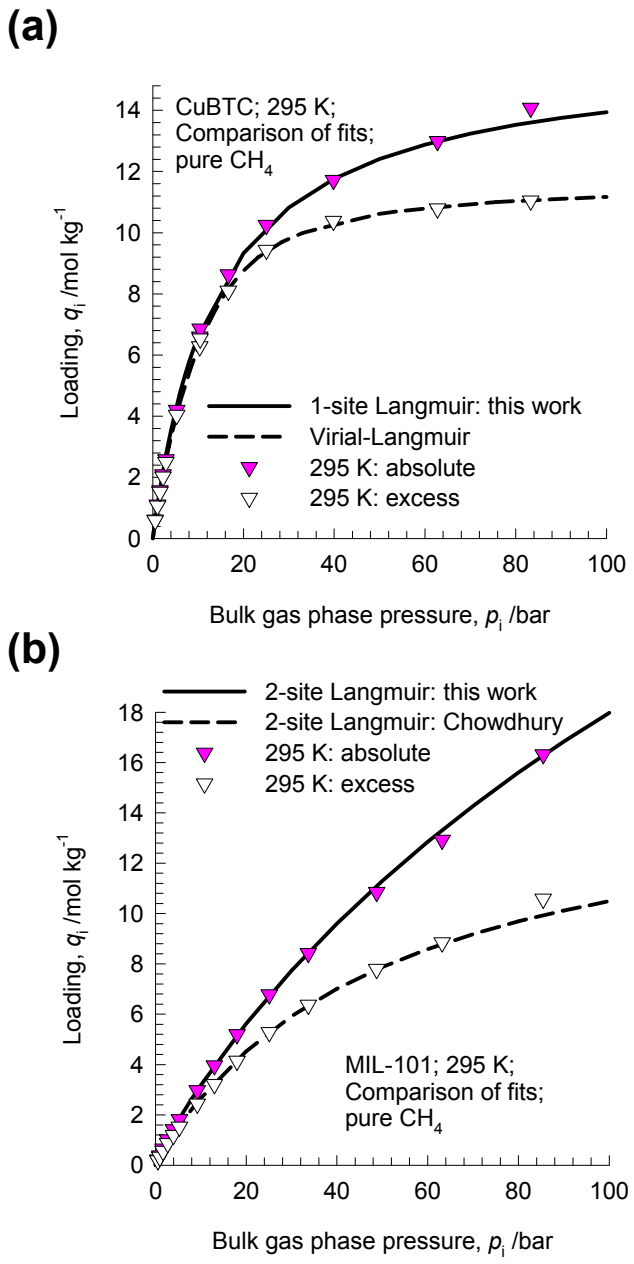
(a)
CuBTC; 295 K;
Comparison of fits;
pure CH4
1-site Langmuir: this work
Virial-Langmuir
295 K: absolute
295 K: excess
Loading, qi /mol kg-1
Bulk gas phase pressure, pi /bar
(b)
2-site Langmuir: this work
2-site Langmuir: Chowdhury
295 K: absolute
295 K: excess
MIL-101; 295 K;
Comparison of fits;
pure CH4
Loading, qi /mol kg-1
Bulk gas phase pressure, pi /bar

Figure 14

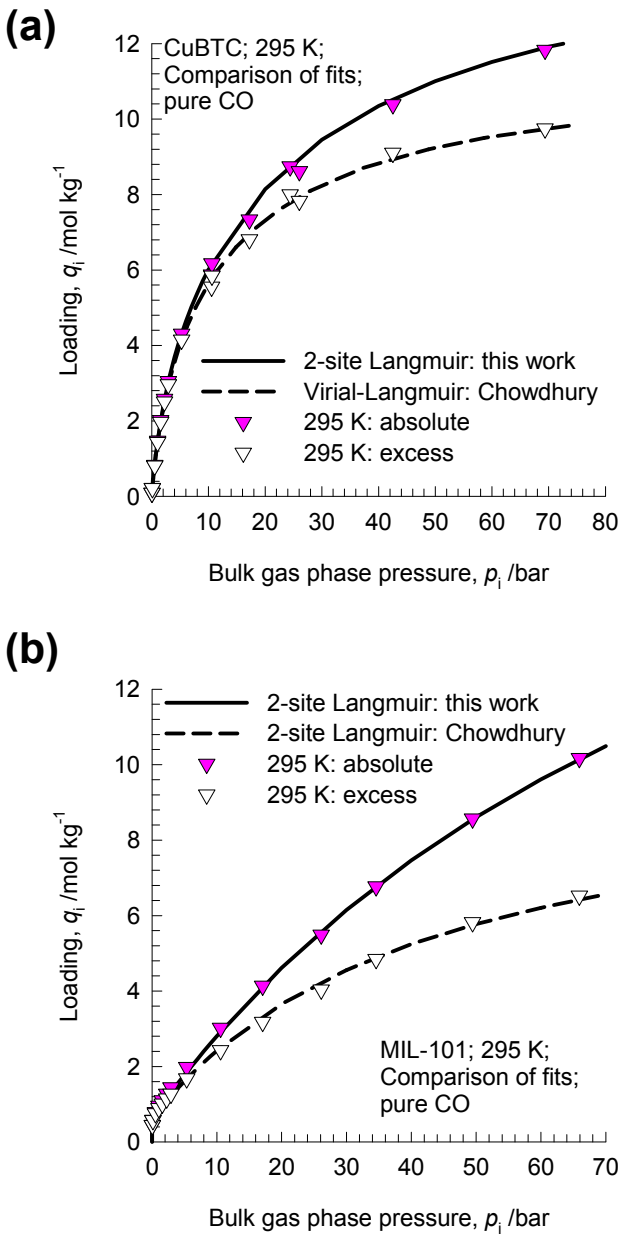
(a)
CuBTC; 295 K;
Comparison of fits;
pure CO
2-site Langmuir: this work
Virial-Langmuir: Chowdhury
295 K: absolute
295 K: excess
Loading, q_i /mol kg^{-1}
Bulk gas phase pressure, p_i /bar
(b)
2-site Langmuir: this work
2-site Langmuir: Chowdhury
295 K: absolute
295 K: excess
MIL-101; 295 K;
Comparison of fits;
pure CO
Loading, q_i /mol kg^{-1}
Bulk gas phase pressure, p_i /bar

Figure 15

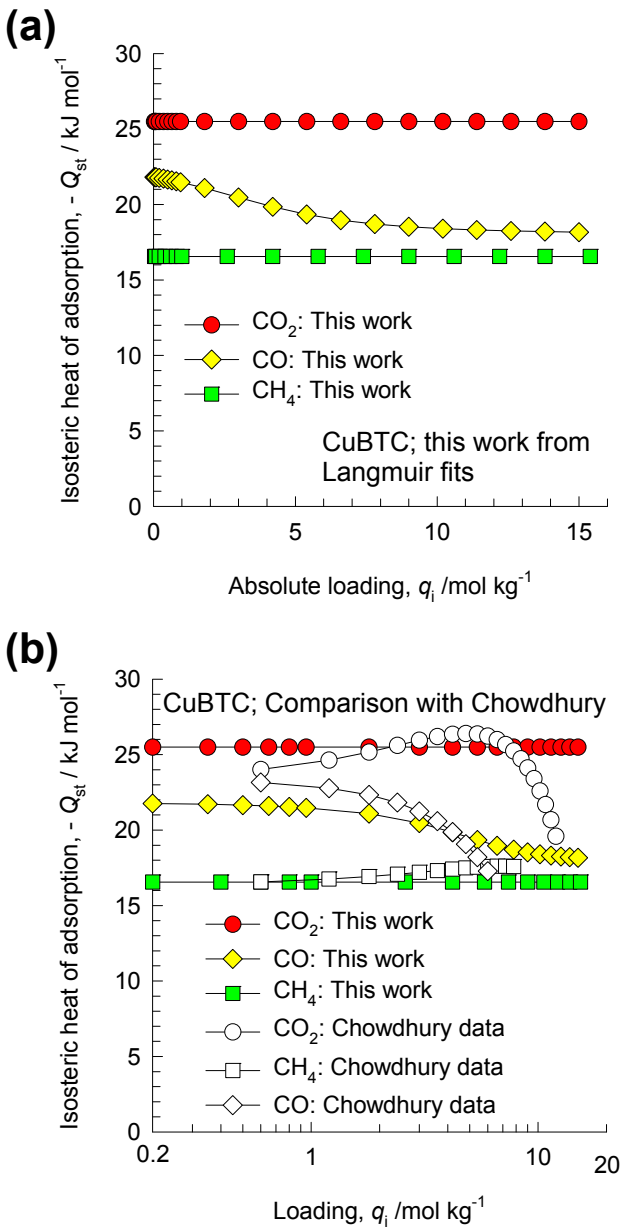
(a)
Isosteric heat of adsorption, - Q_{st} / kJ mol^{-1}
30
25
20
15
10
5
0
0
5
10
15
CO_2: This work
CO: This work
CH_4: This work
CuBTC; this work from Langmuir fits
Absolute loading, q_i /mol kg^{-1}
(b)
Isosteric heat of adsorption, - Q_{st} / kJ mol^{-1}
CuBTC; Comparison with Chowdhury
0.2
1
10
20
CO_2: This work
CO: This work
CH_4: This work
CO_2: Chowdhury data
CH_4: Chowdhury data
CO: Chowdhury data
Loading, q_i /mol kg^{-1}

Figure 16

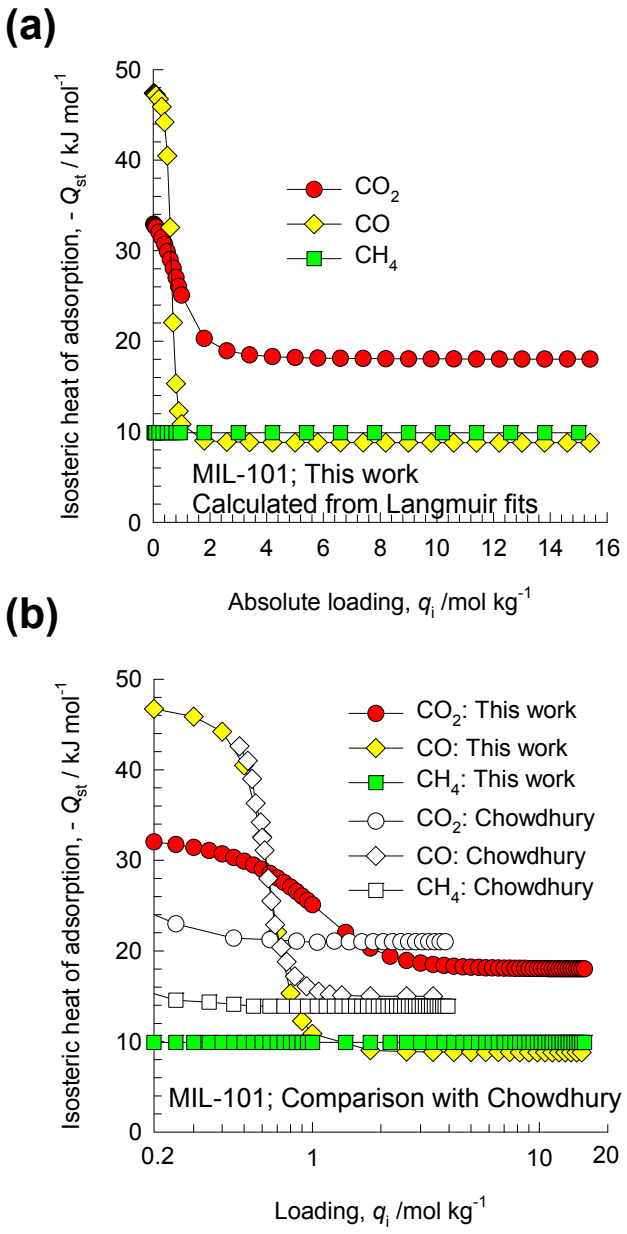
(a)
Isosteric heat of adsorption, - Q_{st} / kJ mol^{-1}
50
40
30
20
10
0
0
2
4
6
8
10
12
14
16
CO_2
CO
CH_4
MIL-101; This work
Calculated from Langmuir fits
Absolute loading, q_i /mol kg^{-1}
(b)
Isosteric heat of adsorption, - Q_{st} / kJ mol^{-1}
50
40
30
20
10
0
0.2
1
10
20
CO_2: This work
CO: This work
CH_4: This work
CO_2: Chowdhury
CO: Chowdhury
CH_4: Chowdhury
MIL-101; Comparison with Chowdhury
Loading, q_i /mol kg^{-1}

Figure 17

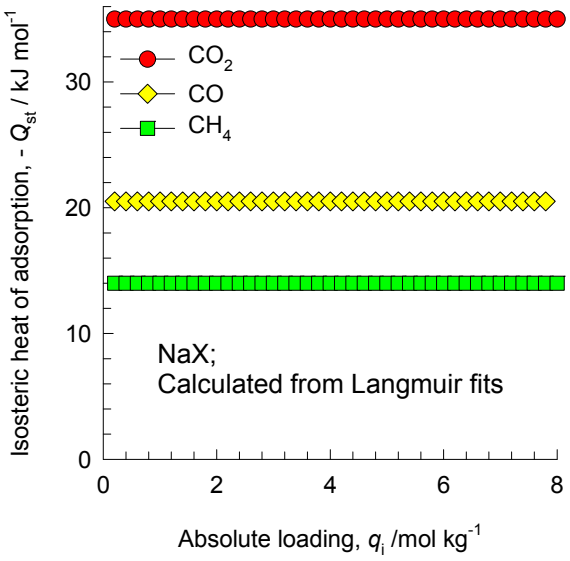
Isosteric heat of adsorption, - Q_{st} / kJ mol^{-1}
Absolute loading, q_i /mol kg^{-1}
CO_2
CO
CH_4
NaX;
Calculated from Langmuir fits
0
10
20
30
0
2
4
6
8

Figure 18

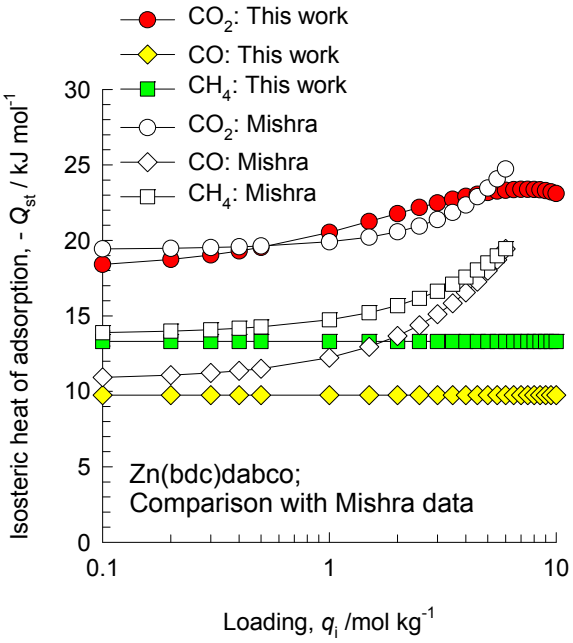
CO2: This work
CO: This work
CH4: This work
CO2: Mishra
CO: Mishra
CH4: Mishra
Isosteric heat of adsorption, - Qst / kJ mol-1
30
25
20
15
10
5
0
0.1
1
10
Zn(bdc)dabco;
Comparison with Mishra data
Loading, qi /mol kg-1

Figure 19

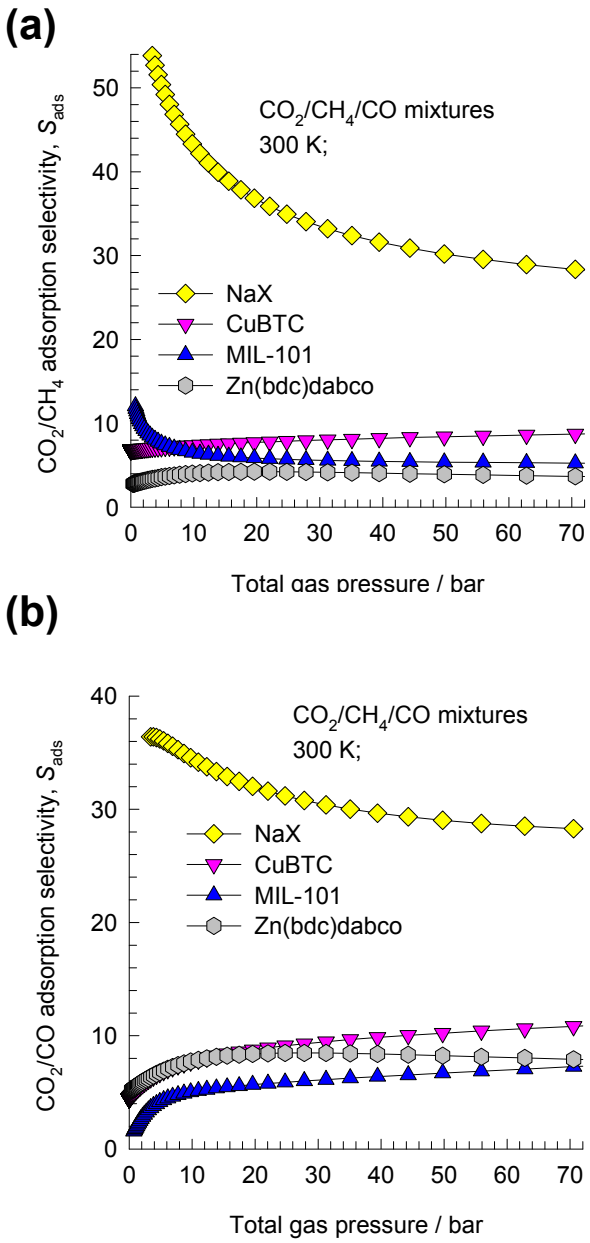
(a)
CO2/CH4/CO mixtures
300 K;
NaX
CuBTC
MIL-101
Zn(bdc)dabco
CO2/CH4 adsorption selectivity, Sads
Total gas pressure / bar
(b)
CO2/CH4/CO mixtures
300 K;
NaX
CuBTC
MIL-101
Zn(bdc)dabco
CO2/CO adsorption selectivity, Sads
Total gas pressure / bar

Figure 20

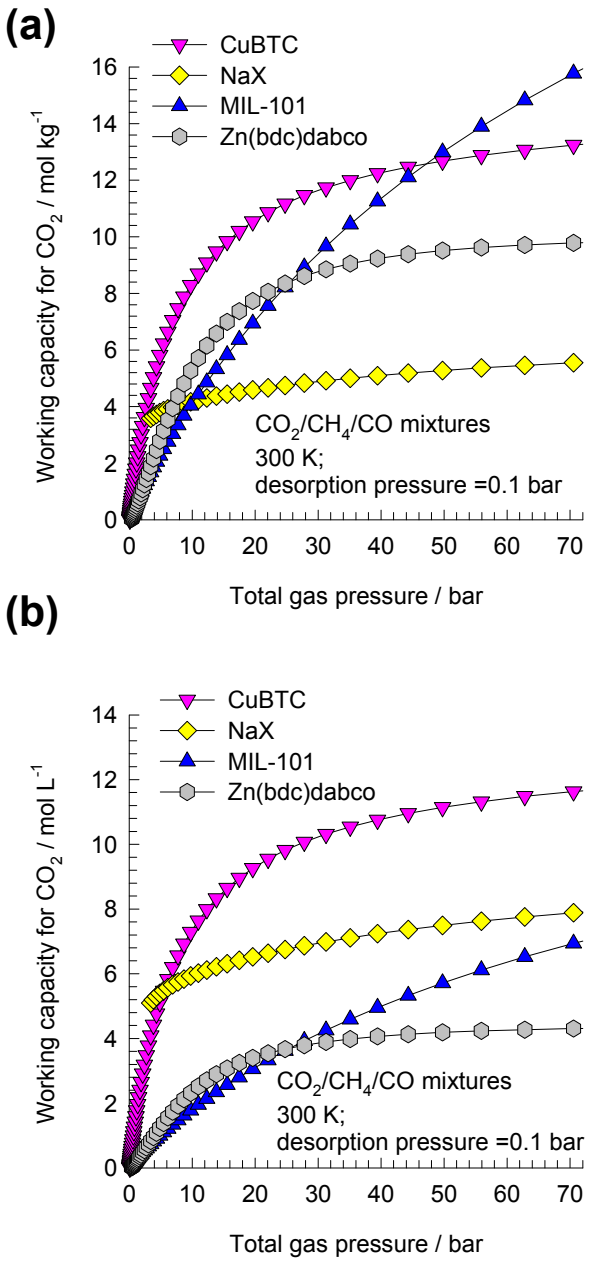
(a)
CuBTC
NaX
MIL-101
Zn(bdc)dabco
Working capacity for CO2 / mol kg-1
CO2/CH4/CO mixtures
300 K;
desorption pressure =0.1 bar
Total gas pressure / bar
(b)
CuBTC
NaX
MIL-101
Zn(bdc)dabco
Working capacity for CO2 / mol L-1
CO2/CH4/CO mixtures
300 K;
desorption pressure =0.1 bar
Total gas pressure / bar

Figure 21

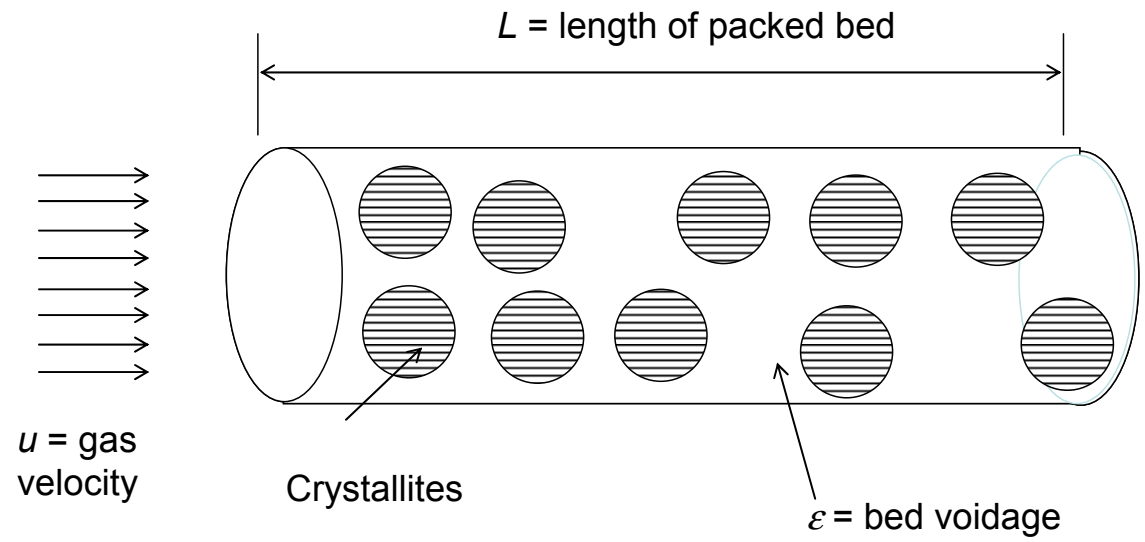

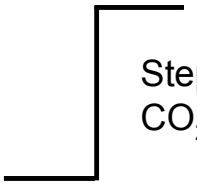

Step input
$CO_2/CH_4/CO$ gas mixture

$L/(u/\varepsilon)$ =
Characteristic time

Figure 22

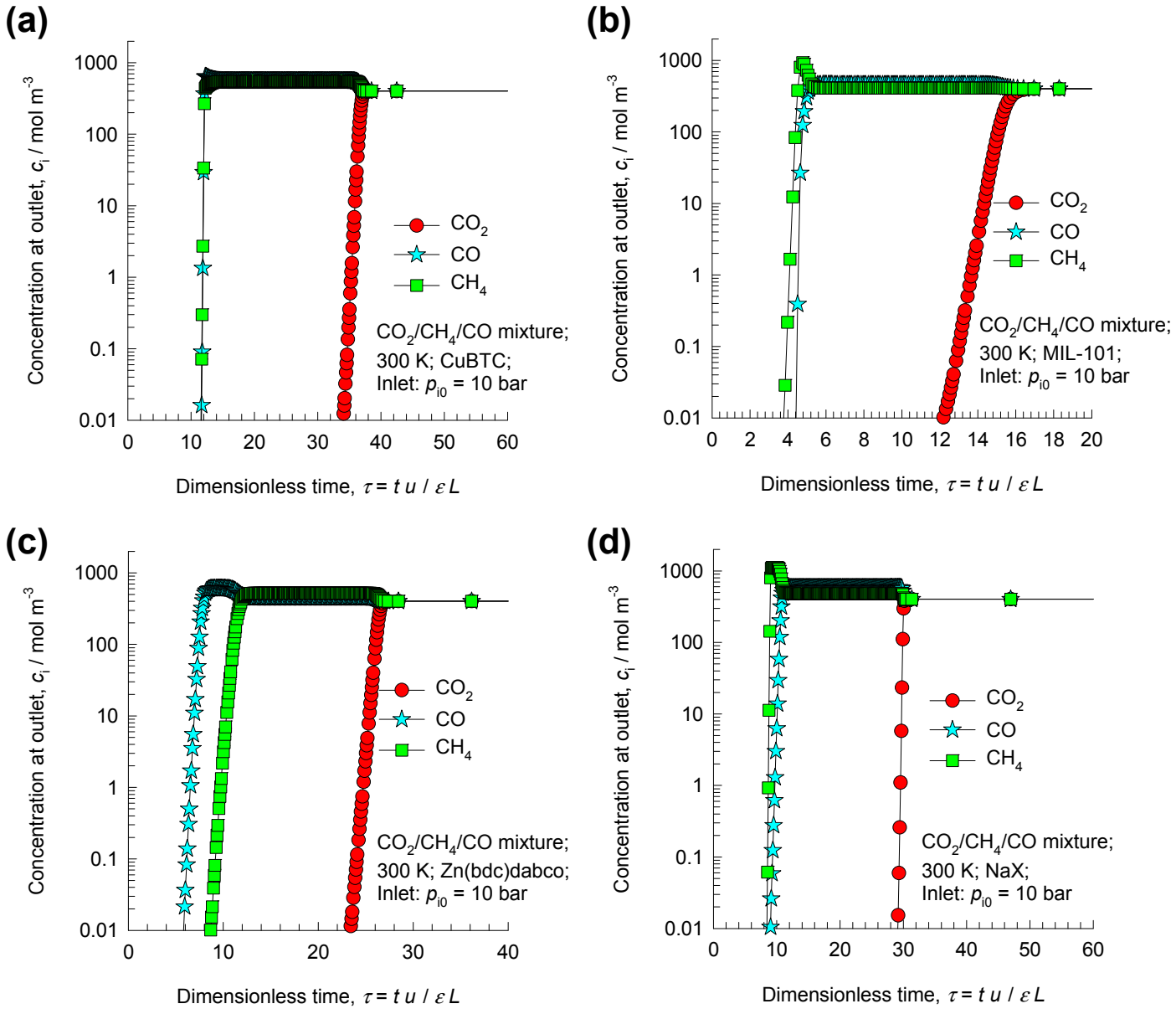
(a)
Concentration at outlet, c_i / mol m^{-3}
1000
100
10
1
0.1
0.01
0
10
20
30
40
50
60
CO$_2$
CO
CH$_4$
CO$_2$/CH$_4$/CO mixture;
300 K; CuBTC;
Inlet: p_{i0} = 10 bar
Dimensionless time, $\tau = t\,u\,/\,\varepsilon\,L$
(b)
Concentration at outlet, c_i / mol m^{-3}
1000
100
10
1
0.1
0.01
0
2
4
6
8
10
12
14
16
18
20
CO$_2$
CO
CH$_4$
CO$_2$/CH$_4$/CO mixture;
300 K; MIL-101;
Inlet: p_{i0} = 10 bar
Dimensionless time, $\tau = t\,u\,/\,\varepsilon\,L$
(c)
Concentration at outlet, c_i / mol m^{-3}
1000
100
10
1
0.1
0.01
0
10
20
30
40
CO$_2$
CO
CH$_4$
CO$_2$/CH$_4$/CO mixture;
300 K; Zn(bdc)dabco;
Inlet: p_{i0} = 10 bar
Dimensionless time, $\tau = t\,u\,/\,\varepsilon\,L$
(d)
Concentration at outlet, c_i / mol m^{-3}
1000
100
10
1
0.1
0.01
0
10
20
30
40
50
60
CO$_2$
CO
CH$_4$
CO$_2$/CH$_4$/CO mixture;
300 K; NaX;
Inlet: p_{i0} = 10 bar
Dimensionless time, $\tau = t\,u\,/\,\varepsilon\,L$

Figure 23

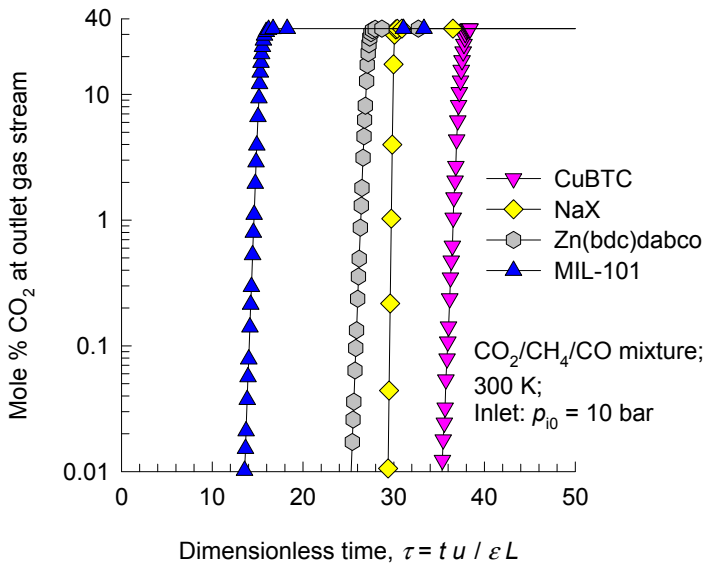
Mole % CO_2 at outlet gas stream
40
10
1
0.1
0.01
0
10
20
30
40
50
Dimensionless time, $\tau = t\,u\,/\,\varepsilon\,L$
CuBTC
NaX
Zn(bdc)dabco
MIL-101
$CO_2/CH_4/CO$ mixture;
300 K;
Inlet: p_{i0} = 10 bar

Figure 24

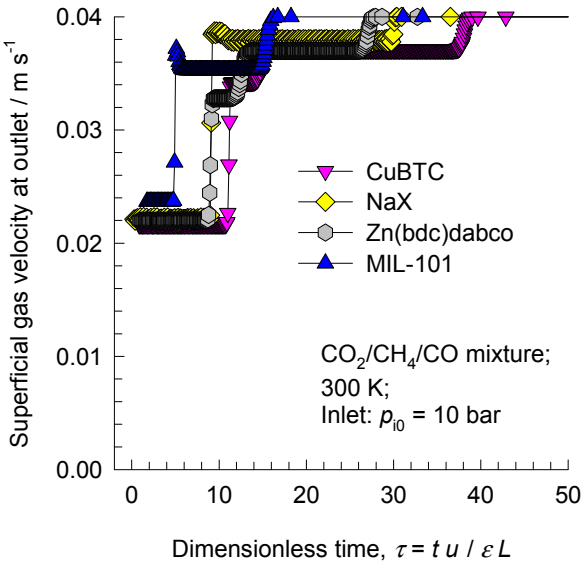
0.04
0.03
0.02
0.01
0.00
0
10
20
30
40
50
Superficial gas velocity at outlet / m s-1
Dimensionless time, τ = t u / ε L
CuBTC
NaX
Zn(bdc)dabco
MIL-101
CO2/CH4/CO mixture;
300 K;
Inlet: pi0 = 10 bar

Figure 25

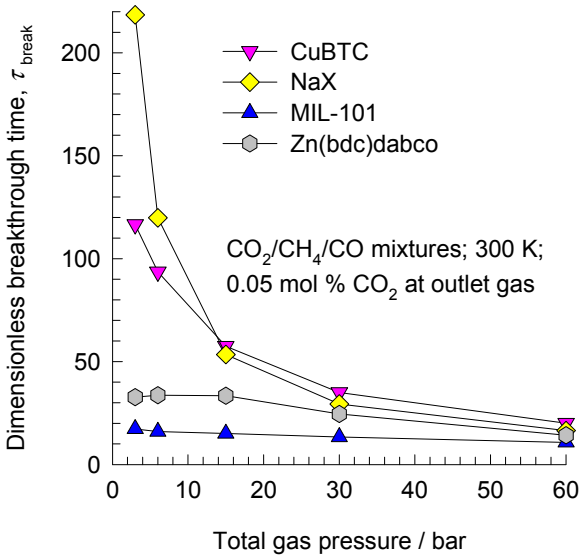
Dimensionless breakthrough time, τ_{break}
200
150
100
50
0
0
10
20
30
40
50
60
Total gas pressure / bar
CuBTC
NaX
MIL-101
Zn(bdc)dabco
$CO_2/CH_4/CO$ mixtures; 300 K;
0.05 mol % CO_2 at outlet gas

Figure 26

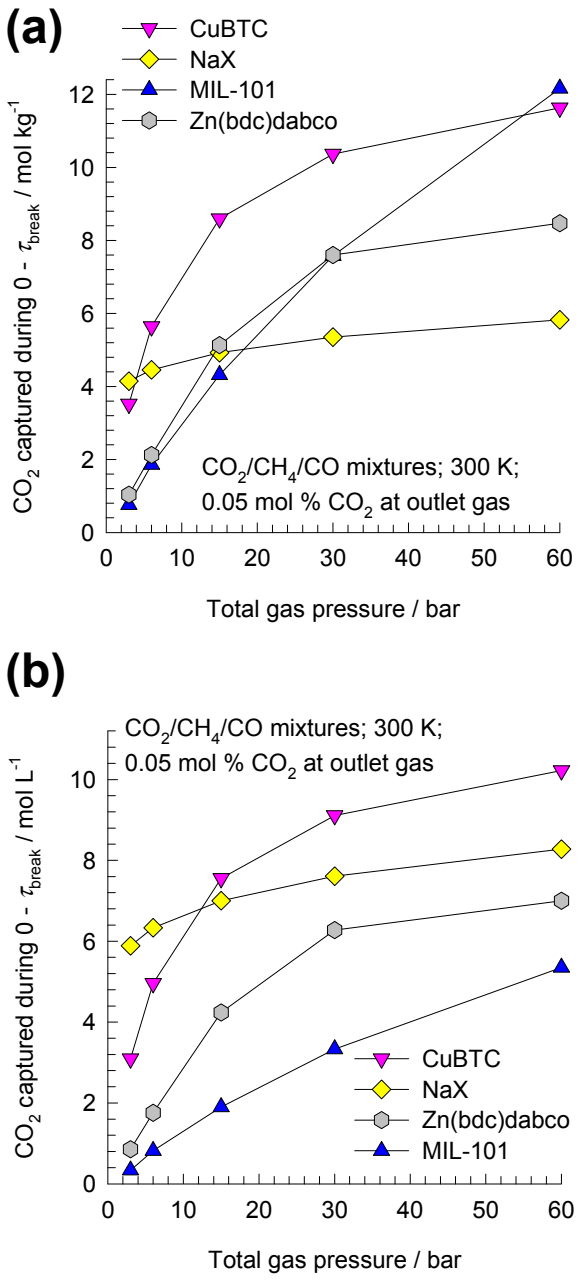
(a)
CuBTC
NaX
MIL-101
Zn(bdc)dabco
CO2 captured during 0 - τbreak / mol kg-1
CO2/CH4/CO mixtures; 300 K;
0.05 mol % CO2 at outlet gas
Total gas pressure / bar
(b)
CO2/CH4/CO mixtures; 300 K;
0.05 mol % CO2 at outlet gas
CO2 captured during 0 - τbreak / mol L-1
CuBTC
NaX
Zn(bdc)dabco
MIL-101
Total gas pressure / bar